The Integrated Precipitation and Hydrology Experiment - Hydrologic Applications for the Southeast US (IPHEx-H4SE)

Part II: Atmospheric Forcing and Topographic Corrections

http://iphex.pratt.duke.edu

Jing Tao and Ana P. Barros

EPL-2013-IPHEX-H4SE-2

December 10, 2013 – V1.0

Acknowledgment: This work was supported by NASA's Precipitation Measurement Missions Program and GPM Ground Validation.

Citation: Tao, J. and Barros, A.P., 2013: The Integrated Precipitation and Hydrology Experiment. Part II: Atmospheric Forcing and Topographic Corrections. Report EPL-2013-IPHEX-H4SE-2, EPL/Duke University (Pub.), V.1., 80pp. DoI: Duke University Libraries (request pending)

Data Availability: http://iphex.pratt.duke.edu

Disclaimer: This purpose of this report is to provide background information on the generation of IPHEX-H4SE data sets. Results are presented for the first five years. The same methods were used for subsequent updating of data sets. This report will be submitted also to peer-review after extensive internal review. Comments and suggestions are welcome.

33

34

35 # Abstract

36

37 In order to prepare atmospheric forcing data sets to drive the hydrologic models at high spatial
38 resolution, it is necessary to apply appropriate downscale methods and bias correction schemes
39 to the coarse reanalysis products. In this manuscript, first we describe the methodology to
40 derive a high-resolution (1×1 km^2, hourly) atmospheric forcing data set from 3-hr NARR (North
41 American Regional Reanalysis) products originally at 32×32km resolution, and second we
42 illustrate the value and utility of the downscaled products to drive hydrologic models offline
43 through analysis of a long-term (5-year) continuous simulation of water and energy budgets in
44 the Southern Appalachians against flux tower observations. The IPHEx-H4SE atmospheric
45 forcing data set includes elevation corrected air temperature and lapse rate, specific humidity,
46 friction velocity, surface layer winds, incoming longwave radiation, and topographically and
47 cloudiness corrected incoming shortwave radiation that enable simulating water and energy
48 fluxes from diurnal to annual time-scales, and for extreme events. Although the 5-year
49 simulation presented here was conducted with a randomly selected rainfall product among those
50 recommended in the companion report (EPL-2013-H4SE-3) without re-initialization or data
51 assimilation, and therefore does not represent an optimal simulation with the hydrological model
52 but rather a baseline control simulation that integrates and propagates the uncertainty in all
53 forcing data sets, the results clearly illustrate the benefit of using the bias corrected NARR
54 atmospheric forcing fields made available here.

1. Introduction

The IPHEx-H4SE project (Integrated Precipitation and Hydrology Experiment – Hydrologic Applications for the Southeast US) is the first ground-validation field campaign planned after the launch of the Global Precipitation Measurement Mission satellite launch *(GPM,* www.nasa.gov/mission_pages/GPM*).* The field campaign comprehends intense data collection activities aimed at acquiring observational data to evaluate and improve GPM precipitation estimation algorithms, as well as hydrologic modeling activities focusing on evaluating the utility of satellite-based rainfall products for hydrologic applications including water resources management and forecasting of natural hazards such as flash floods, riverine floods and landslides. The hydrologic modeling activities in turn consist of real-time forecasting activities during the Intense Observing Period of the IPHEx field campaign April-July 2014, and a collaborative effort (H4SE) envisioned as a benchmark to facilitate inter-comparison of hydrologic models and evaluation of rainfall estimation algorithms. The hydrologic applications will be conducted without coupling to a weather or climate prediction model, therefore in the so-called off-line mode. A common data set concerning atmospheric forcing and landscape attributes is provided to all H4SE participants. The data sets span four drainage basins of interest in the IPHEx-H4SE with headwaters in the Southern Appalachians: Upper Tennessee River Basin (UTRB), Savannah River Basin (SVRB), Santee River Basin (SRB) and Yadkin-Pee Dee River Basin (YPDRB), as shown in Figure 1d. H4SE participants agree to conduct a selected number of case studies and provide their results to the project to be analyzed jointly and to be co-authors in related synthesis publications, and may or may not participate in the operational forecasting activities during IPHEx.

In this manuscript, we present the development of atmospheric forcing datasets at high-resolution (1×1 km^2, hourly). The data were derived from the North American Regional Reanalysis (NARR) products originally at 32-km spatial resolution and 3-hour temporal resolution (Mesinger et al., 2006). The standard atmospheric datasets required for hydrologic models typically include air temperature, air pressure, wind velocity, specific humidity and downward radiation (shortwave/solar radiation and longwave/thermal radiation). The air temperature, air pressure, wind velocity and specific humidity time-series should be available at least one common measurement height (10m in this project). Previous studies have demonstrated that the bias correction applied to reanalysis products, especially in the case of atmospheric forcing data to drive land surface hydrological models, can affect the simulations of hydrological fluxes significantly (Berg et al., 2003; Lenters et al., 2000). Thus, appropriate downscale methodology correctly disaggregating atmospheric variables at coarse resolution to the fine resolution required by hydrologic models is of vital importance. Schomburg et al. (2010) proposed a downscaling scheme based on statistical characteristics of atmospheric near-surface variables at different scales for disaggregating atmospheric forcing data for a soil–vegetation–atmosphere transfer (SVAT) model. Gao et al. (2012) applied an elevation correction method to downscale 3-hourly ERA-Interim air temperature data using internal vertical lapse rates derived from different ERA-Interim pressure levels in complex terrain. Berg et al. (2003) reported that the implementation of a bias reduction scheme to air temperature, dew point temperature, surface pressure, precipitation, shortwave and longwave radiation from the European Centre for Medium Range Weather Forecasts (ECMWF) 15-year reanalysis (ERA) and to the National Center for Environmental Prediction/National Center for Atmospheric Research (NCEP/NCAR) reanalysis

99 (NRA), reduced the errors in simulations of soil moisture, runoff and snow water equivalence
100 using a catchment-based land surface model (CLSM).

101 The methodology based here was inspired by the approach used for the development of
102 forcing datasets for NLDAS-2 (12×12 km^2 resolution, North American Land Data Assimilation
103 System, e.g. Cosgrove et al. (2003)). However, due to the much higher spatial and temporal
104 resolution requirements, there are significant differences between the topographic and cloudiness
105 corrections used here, as well as interpolation criteria, and those used in NLDAS2. Specifically,
106 elevation adjustments and corrections to near-surface variables including air temperature, air
107 pressure, specific humidity and longwave radiation, were applied between NARR terrain and
108 local terrain at every time-step based on predicted atmospheric conditions (e.g. using dynamic
109 lapse rates) instead of using average values or monthly time-scales. The dynamic lapse rates
110 were derived from the NARR atmospheric temperature profiles using the isobaric levels closest
111 to the NARR terrain and the local DEM at high resolution, and then were applied to correct
112 atmospheric temperature first, followed by the air pressure, specific humidity and longwave
113 radiation. To downscale the wind velocity from NARR coarse resolution to 1×1 km^2, we
114 adjusted friction velocity based on an empirical relationship between the geostrophic drag
115 coefficients and the Rossby Number proposed by Lettau (1959).

116 Special bias corrections for downward shortwave radiation are applied through dynamical
117 adjustment, accounting for cloudiness and topographic effects. The downward shortwave
118 radiation at the surface is of vital importance the energy exchange between the atmosphere and
119 the surface, influencing the efficiency of photosynthesis in biosphere. The accurate real-time (up
120 to hourly) shortwave radiation at high resolution is essential for hydrological applications,
121 because radiative forcing drives water transfers and energy fluxes. NARR downward shortwave

(SW) radiation at surface provide 3-hour incoming SW radiation flux at about 0.3deg (32km), which show large bias especially in topographically complex regions (Pinker et al., 2003; Schroeder et al., 2009). The NLDAS-2 primary forcing data includes bias-correction of NARR downward shortwave radiation based on a ratio-based bias correction method at monthly time-scales (Berg et al., 2003). In their method, the ratio was calculated using the monthly mean diurnal cycle of downward shortwave radiation from the GEWEX Continental Scale International Project (GCIP) Surface Radiation Budget (SRB-GCIP) dataset (Pinker et al., 2003) to the monthly mean values from NARR dataset, and then it was applied to correct hourly NARR radiation linearly interpolated in time from the 3-hourly NARR data. To downscale the NARR incoming shortwave radiation to high spatial resolution for H4SE, the cloudy effects and the topographic effects have to be explicitly accounted for in real-time because of the rapid evolution and transformation of cloud systems. Based on a topographic solar radiation model (Dozier, 1980; Dozier and Frew, 1990), a topographic radiation correction technique was developed (Dubayah et al., 1990; Dubayah and Loechel, 1997) and has been widely applied. A similar correction technique is adapted to downscale 32km NARR incoming solar radiation data to 1km resolution at monthly scale (Schroeder et al., 2009). Here, we present a methodology for cloudiness and topographic correcting and downscaling 3-hr NARR incoming shortwave radiation at 32km resolution to hourly data at 1km resolution based on the technique developed by Dubayah and Loechel (1997), relying on the accurate SRB-GCIP dataset for retrieving shortwave atmopshere transmittance and real-time cloudiness pattern. This method accounts for both the cloudy effects and the terrain effects, i.e. regional cloudiness pattern, cast-shadow caused by sun-blocking terrain, self-shadow, and the reflected shortwave radiation from the

surrounding terrain. This leads to significant improvements especially in the topographically complex terrain such as the Southern Appalachian Mountains.

The adjusted atmospheric forcing datasets, including the atmospheric temperature, atmospheric pressure, specific humidity, wind speed at 10m above the ground, and the downward shortwave and longwave radiation at surface, were compared with available tower observations, as well as with the NLDAS-2 primary forcing data (Mitchell et al., 2004; Xia et al., 2012a; Xia et al., 2012b). The premise in deriving these data sets is that some hydrologic models may require calibration and therefore in order to avoid spurious model sensitivities an effort is made to generate atmospheric forcing that can capture the diurnal cycle as well as seasonal and inter-annual variability, in addition to extreme events. The utility of these atmospheric forcing datasets in hydrological applications has been demonstrated in the basin featuring the most complex terrain among the four drainage basins in the IPHEx-H4SE, the Upper Tennessee River Basin (UTRB). Five-year continuous hydrological simulations were conducted in a headwater basin to the UTRB, the Pigeon River Basin in the Southern Appalachians (illustrated in Figure 1d), using a distributed hydrological model (3D-LSHM) (see report EPL-IPHEX-H4SE-3).

2. Methodology and Procedure

2.1 Elevation Corrections

NARR terrain shows a smooth elevation envelope differing very much from the local elevation at high resolution, especially in the mountainous region, as shown by Figure **1**. The maximum difference between the NARR terrain and the local DEM is up to 1064m at the ridge lines of the Pigeon River Basin. To account for such significant elevation difference, the elevation correction

166 to the NARR fields has to be performed before they are used as forcing datasets in hydrological
167 studies. In this study, the three-hour atmospheric temperature, atmospheric pressure, specific
168 humidity at 10m above ground (ABG) and downward longwave radiation at surface originated
169 from NARR were corrected for elevation effects, adopting the similar assumptions and
170 methodology as in the study of Cosgrove et al. (2003). All of these NARR fields at about 32km
171 were bi-linearly interpolated to 1km first. The NARR terrain geometric height was also
172 interpolated to 1km, to calculate the elevation difference at 1km between the NARR terrain and
173 the local 1km DEM sampled from SRTM data[1] at about 90m spatial resolution. High-resolution
174 elevation corrections (topographic adjustment) require spatially-temporally dynamic lapse rates
175 for adjusting atmospheric temperature [a constant lapse rate (-6.5K/km) was used in Cosgrove et
176 al. (2003)]. Then the atmospheric pressure, specific humidity and downward longwave radiation
177 were corrected sequentially. The lapse rate was calculated from the NARR atmospheric
178 temperature profile at low isobaric levels (1000mb to 800mb) at each pixel (1km grid element) at
179 each time step (3-hour). Instead of using NARR terrain as the reference level, the two closest
180 geometric heights converted from the geopotential heights at isobaric levels to the NARR terrain
181 and the local DEM were utilized to calculate lapse rate, which is used next to adjust atmospheric
182 temperature from the NARR terrain to the local DEM at 1km. A flowchart describing the
183 procedures applying the elevation correction to NARR fields is given in Figure 2.

184 The adjusted atmospheric temperature is calculated by

$$T_{adj} = T_{NARR} + \gamma \Delta z \qquad (1)$$

[1] http://srtm.csi.cgiar.org/SELECTION/inputCoord.asp

where T_{adj} is the adjusted atmospheric temperature at 10m ABG (K), T_{NARR} is the original NARR atmospheric temperature at 10m ABG (K), γ is the lapse rate (K/km) and Δz is the elevation difference between the NARR terrain and the DEM data at 1km. The lapse rate γ varies depending on the atmospheric conditions, for instance, the γ in the early morning is very different from the γ at noon, and the γ in the mountainous region also differs from that in the plain area. Thus, we calculate the lapse rate at each NARR time step (3hr) at each 1km pixel over the southeast US. Figure 3 illustrates examples of calculating lapse rate using atmospheric temperatures and geometric heights converted from the geopotential heights at selected isobaric levels closest to the NARR terrain and local DEM. For instance as shown in Figure 3(a), the height at 900mb which is the closest level to the NARR terrain and the heights at 925mb level which is the closest one to the DEM, were chosen to calculate the lapse rate, resulting in a quite large lapse rate γ as -3.28K/km. In Figure 3(b), for a pixel that the DEM is much larger than NARR terrain, the heights and temperatures at 875mb and 900mb were chosen to calculate and obtain a lapse rate γ as -7.91K/km. Figure 3(c) demonstrates the elevation correction to the NARR atmospheric temperature along a transect line as illustrated in Figure 1(c) starting from the Tennessee Valleys and right crossing the Blue Ridge Mountains to the Coastal plain in the southeast corner of the region. As can be seen from Figure 3(c), the adjusted atmospheric temperatures show significant difference from the original NARR atmospheric temperature in the mountainous region (up to 6K), although the difference in temperature is not very large in the flat areas due to the small elevation difference between the NARR terrain and the DEM.

Similar to Cosgrove et al. (2003), from the ideal gas law $p = \rho RT$ and the hydrostatic approximation $\frac{\partial p}{\partial z} = -\rho g$, we arrive at

$$\frac{RT\partial\rho}{\rho g} = -\partial z \tag{2}$$

where p is the atmospheric pressure (Pa), ρ is the atmosphere density (kg/m^3), R is the gas constant, and T is the atmospheric pressure (K). Integrating both sides of the equation (2), we obtain,

$$\Delta z = -\frac{RT_{mean}}{g} ln\left(\frac{p_{adj}}{p_{NARR}}\right) \tag{3}$$

where T_{mean} is assumed to be the average of T_{adj} andT_{NARR}, $p_{adj}$is the adjusted atmospheric temperature at 10m above the DEM (Pa), $p_{NARR}$is the original NARR atmospheric temperature at 10m above the NARR terrain (Pa). Thus p_{adj} can be derived by rearranging equation (3),

$$p_{adj} = \frac{p_{NARR}}{exp\left(\frac{g\Delta z}{RT_{mean}}\right)} \tag{4}$$

Assuming a constant relative humidity throughout the Δz, and thus $RH = \frac{q_{NARR}}{q_{sat_{NARR}}} = \frac{q_{adj}}{q_{sat_{adj}}}$, we finally arrive at

$$q_{adj} = q_{sat_{adj}} \frac{q_{NARR}}{q_{sat_{NARR}}} \tag{5}$$

where q_{adj} and $q_{sat_{adj}}$ are respectively the adjusted atmospheric specific humidity and the adjusted saturated specific humidity, and q_{NARR} and $q_{sat_{NARR}}$ are the original NARR specific humidity and the original NARR saturated specific humidity, respectively. The saturated specific humidity can be calculated as:

$$q_{sat_{adj}} = \frac{0.622 e_{sat_{adj}}}{p_{adj} - 0.378 e_{sat_{adj}}} \quad (6)$$

$$q_{sat_{NARR}} = \frac{0.622 e_{sat_{NARR}}}{p_{adj} - 0.378 e_{sat_{NARR}}} \quad (7)$$

where $e_{sat_{adj}}$ and $e_{sat_{NARR}}$ is the adjusted and the original NARR saturated water vapor pressure which can be estimated by Wexler's equation.

Lastly, the adjusted downward longwave radiation is calculated based on the Stefan-Boltzmann law,

$$LW_{adj} = \frac{\varepsilon_{adj}\sigma}{\varepsilon_{NARR}\sigma}\left(\frac{T_{adj}}{T_{NARR}}\right)^4 LW_{NARR} \quad (8)$$

where $\sigma$is the Stefan-Boltzman constant, LW_{adj} and LW_{NARR} are respectively the adjusted and the original NARR downward longwave radiation at surface(W/m^2), and likewise ε_{adj} and ε_{NARR} are the adjusted and the original NARR emissivity at longwave. The same simplified equations as in Cosgrove et al. (2003) are used to calculate emissivity here based on vapor pressure, to make the adjustment to the atmospheric emissivity,

$$\varepsilon_{adj} = 1.08 \times \left\{1 - exp\left(-e_{adj}^{T_{adj}/2016}\right)\right\} \quad (9)$$

$$\varepsilon_{NARR} = 1.08 \times \left\{1 - exp\left(-e_{NARR}^{T_{NARR}/2016}\right)\right\} \quad (10)$$

where $e_{adj}$and e_{NARR} is the adjusted and the original NARR vapor pressure (hPa), calculated by $e_* = (q_* p_*)/0.622$ where * denotes either 'adj' or 'NARR'.

2.2 Wind Adjustment

For the wind adjustment, we follow Lettau's work on the dependence of geostrophic drag coefficient on surface roughness (Lettau, 1959). We consider two spatial scales of interest: the geostrophic (synoptic) scale, and the mesoscale that depends on the topography (i.e. the roughness length at the scale of interest) and the Coriolis acceleration. The geostrophic drag coefficient at a scale L can be expressed as $C_g = \frac{u_*}{U_g}$, where u* is the surface layer friction velocity at the same scale L, and $U_g$is the geostrophic wind. Based on a number of balloon measurements, Lettau (1959) proposed an empirical relationship between the geostrophic drag coefficients and the Rossby Number:

$$C_g = 0.16{R_o}^{-0.09} \tag{11}$$

The Rossby Number R_o is equal to $\frac{U_g}{fz_0}$, where f is the Coriolis acceleration and $z_0$is the roughness length at scale L. The Rossby Number is of the order of magnitude of the ratio of a geostrophic to geostrophic winds, and thus is a metric of the relative role of the pressure gradient force (that drives the geostrophic wind) and the Coriolis force. Replacing R_o with $\frac{U_g}{fz_0}$ in equation (11), we arrive at,

$$0.16\left(U_g\right)^{0.91} = u_*(fz_0)^{-0.09} \tag{12}$$

Assuming U_g is the same at the NARR resolution scale L (=32km) and at the local smaller scale ι (1km), then the right-hand side of equation (12) is a constant, and thus we obtain the relationship between friction velocity at different scales,

$$u_*^L (fz_0^L)^{-0.09} = u_*^\iota (fz_0^\iota)^{-0.09} \quad (13)$$

Therefore, the friction velocity at scale ι is related to the friction velocity at scale L,

$$u_*^\iota = u_*^L \left(\frac{z_0^L}{z_0^\iota}\right)^{-0.09} \quad (14)$$

where the roughness length at scale L is provided by NARR, the friction velocity u_*^L is retrieved by the NARR wind speed at 10 meter and at 30 meter based on the logarithm profile law of wind speed. Then, using the logarithm profile law to express wind speed in the boundary layer, the adjusted wind speed at scale ι is expressed as,

$$U^\iota = \frac{u_*^\iota}{k} \log\left(\frac{10-d}{z_0^\iota}\right) \quad (15)$$

where k is the Von Kármán constant (~0.41), and the roughness length z_0^ι and the displacement height d depend on the landcover at the same scale (1km).

2.3 Topographic and Cloudiness correction to downward shortwave radiation

The topographic radiation correction technique includes four stages as illustrated in Figure 4: A) Preprocessing, B) Preparation for auxiliary input parameters, C) Cloudiness correction, and D) Topographic correction.

A) ***Preprocessing*** - The preprocessing mainly involves re-projecting all the radiative fluxes to UTM 17N (WGS84) coordinates and spatially bi-linearly interpolating the data to 1km resolution. The spatially interpolated data are then interpolated from NARR SW in time (3-

hourly to hourly) based on the real-time solar zenith angle. This step is similar to (Cosgrove et al., 2003). However, the temporal interpolation method using the solar zenith angle only cannot account for cloudy conditions. We propose a modified methodology for temporal interpolation that incorporates the diurnal cycle of NARR cloudiness, meanwhile preserving the total daily energy. After the temporal interpolation is complete, the cloudiness and topographic correction is applied to the hourly incoming shortwave radiation. The hourly SW radiation interpolated from 3-hour NARR SW radiation can be expressed by,

$$\mathrm{SW_{ij}} = \mathrm{SW_{tot}}\left(\frac{\sqrt{\mathrm{SW_i^{NARR}}\cos\varphi_\mathrm{i}}}{\sum_{\mathrm{i=1}}^{8}\sqrt{\mathrm{SW_i^{NARR}}\cos\varphi_\mathrm{i}}}\right)\left(\frac{\cos\varphi_\mathrm{ij}}{\sum_{\mathrm{j=1}}^{3}\cos\varphi_\mathrm{ij}}\right) \quad (16)$$

where i is from 1 to 8 as the total daily number of 3-hour intervals in the NARR data, indicating the ith 3-hour interval, j varies from 1 to 3, indicating the jth hour within each 3-hour interval ; $cos\varphi_{ij}$ is the cosine of solar zenith angle at the jth hour within the ith 3 hour; SW_{tot} is the daily total energy (a local diurnal cycle); SW_i^{NARR} is the original NARR 3-hour mean SW radiation for the ith 3 hour, and $cos\varphi_i$ is the mean cosine of solar zenith angle at the three hours within the ith 3 hour, i.e. $cos\varphi_i = \frac{1}{3}\sum_{j=1}^{3} cos\varphi_{ij}$. In this way, the hourly shortwave radiation depends not only on the local solar zenith angle, but also on the NARR simulated cloudiness by incorporating the SW_i^{NARR}.

Then, the new interpolated 3-hour mean SW radiation for the i^{th}3 hour is given by

$$SW_i = \sum_{j=1}^{3} SW_{ij} = \sum_{j=1}^{3} SW_{tot} \left(\frac{\sqrt{SW_i^{NARR} cos\varphi_i}}{\sum_{i=1}^{8} \sqrt{SW_i^{NARR} cos\varphi_i}} \right) \left(\frac{cos\varphi_{ij}}{\sum_{j=1}^{3} cos\varphi_{ij}} \right) =$$

$$SW_{tot} \left(\frac{\sqrt{SW_i^{NARR} cos\varphi_i}}{\sum_{i=1}^{8} \sqrt{SW_i^{NARR} cos\varphi_i}} \right) \sum_{j=1}^{3} \left(\frac{cos\varphi_{ij}}{\sum_{j=1}^{3} cos\varphi_{ij}} \right) = SW_{tot} \left(\frac{\sqrt{SW_i^{NARR} cos\varphi_i}}{\sum_{i=1}^{8} \sqrt{SW_i^{NARR} cos\varphi_i}} \right) \quad (17)$$

B) ***Preparation for auxiliary input parameters*** – In addition to the transmittance and spatial statistic characteristics of solar radiation that are also needed to calculate based on hourly SRB data, other auxiliary input parameters including a sky view factor, terrain configuration factor, hourly local illumination angle and actual surface albedo have to be calculated beforehand in order to correct the topographic effects for shortwave radiation. The actual albedo of the land surface is a weighted average of the black-sky albedo (BSA) and white-sky albedo (WSA). The weighting coefficient is the fraction of diffuse skylight depending on solar zenith angle, optical depth, local aerosol type, etc. (Schaaf et al., 2002). The hourly BSA and WSA were calculated using solar zenith angle and the BRDF model parameters provided in the MODIS product (MCD43B1). The fraction of diffuse skylight was read from a lookup table[2] according to local solar zenith angle, optical depth, aerosol model type and MODIS bands (0.25-4.00 µm). The detailed description is provided in the companion paper (Tao and Barros 2013b- Part X). The sky view factor represents the total portion of unobstructed sky visible on a slope in all directions, with a value of one indicating that the sky is unobstructed and zero meaning the sky is completely obstructed by surrounding topography. For instance, the sky view factor is very small at the bottom of narrow valleys meaning the valley receives less diffuse radiation because a part of the sky hemisphere is blocked by the nearby terrain. The terrain configuration factor indicates

[2] http://www-modis.bu.edu/brdf/userguide/tools.html

298 the fraction of the surrounding terrain visible to a pixel that receives the reflected radiation from
299 the visible terrain. A terrain configuration factor of unity means that only terrain is visible. The
300 local illumination angle plays an important role for quantifying the effects of self-shadowing and
301 reducing the incoming direct irradiance, i.e. when the Sun is below the local horizon of the slope.

302 Another required input parameter is the shortwave transmittance for partitioning the direct and
303 diffuse radiation. We calculated the transmittance using the ratio of the hourly SRB-GCIP
304 downward solar radiation at the surface to the radiation at the top-of-atmosphere (TOA). The
305 derived transmittance is assumed to be representative of the atmospheric conditions in which just
306 part of the radiation is transmitted through the atmosphere. The transmittance will be used to
307 partition the total NARR SW shortwave radiation into direct and diffuse components. However,
308 SRB-GCIP does not provide data for early morning and later afternoon at lower cosine of solar
309 zenith angle, i.e. solar zenith angle larger than 70°(Cosgrove et al., 2003). Consequently, a filling
310 strategy based on the assumption that the cosine of solar zenith angle can be approximated by the
311 shortwave transmittance to the first order was implemented (Chavez, 1996). This approximation
312 works best at dawn or dust, when the incoming solar radiation is also very small. On average,
313 transmittance largely depends on the light path, thus on solar zenith angle. But note that, this
314 approximation is limited to the situation when the solar zenith angle is less than 55°. In reality,
315 highly non-linear relationships exist between transmittance and the cosine solar zenith angle over
316 the full range of solar zenith angles. The nonlinearity is attributed to non-uniform cloudy
317 conditions. The filling steps adopted here are as follows: 1) first use the downward solar
318 radiation at the top-of-atmosphere and at the surface to calculate the raw transmittance; 2) then if
319 partial transmittance data over the whole region exists but the locally is missing, the spatial
320 filling was performed first using the nearest non-missing transmittance multiplied by the ratio of

cosine of the solar zenith angle at the missing pixel to the cosine of the solar zenith angle at the non-missing pixel; 3) Temporal filling was performed for the transmittance in early morning and late afternoon using the closest available data, e.g. using transmittance at 9am to fill the missing data in 6am~8am, also based on the ratio of cosine of the solar zenith angles. 4) the final transmittance is the average of spatially filled and temporally filled transmittance, to account for the variability both in space and time. If the whole region misses the SRB completely, i.e. no partial data exist, only temporal filling is necessary and the temporally filled transmittance is the final transmittance.

C) ***Cloudiness correction*** - For a clear situation, the topographic effects dominate the spatial variability of incoming solar radiation. While for a cloudy situation, it is the cloudiness pattern that determines the spatial distribution of the solar radiation. In order to account for real-time cloudiness patterns, we rely on the SRB again. Specifically, we calculated the PDF of both the spatial SRB solar radiation and the NARR shortwave radiation, then we match the PDF of the NARR shortwave radiation to that of the SRB data, by calculating a histogram index at each pixel, $\lambda(i,j) = (R^S_{max} - R^S(i,j))/(R^S_{max} - R^S_{min})$ where $R^S(i,j)$ is the SRB solar radiation at pixel (i,j), $R^S_{max}$and $R^S_{min}$is the maximum and minimum value of the spatial SRB solar radiation at current time, respectively. The regional cloudiness pattern is represented by $\lambda(i,j)$ depicting a position at the histogram scale. Therefore, using the histogram index $\lambda(i,j)$, we reshuffle the NARR SW radiation by matching its PDF to SRB's PDF, $R(i,j) = R_{max} - \lambda(i,j)(R_{max} - R_{min})$ where the $R(i,j)$ is the new NARR SW radiation accounted for the cloudiness pattern, R_{max} and R_{min} are the maximum and minimum value of the spatial NARR SW radiation at the current time. Note, now the NARR SW radiation at pixel (i,j) is at the same position at its histogram scale as that at the SRB histogram scale, i.e. matching the PDF of NARR to SRB's, as

shown in Figure 5. As it can be seen from the figure, (c.2) shows the exact same PDF shape as (b.2) which is the spatial PDF of SRB, i.e. showing the same cloudiness pattern as the SRB data (illustrated by c.1 versus b.1), while maintaining the original range of NARR SW radiation (c.2) over the region.

D) ***Topographic correction*** - To downscale radiation from coarse resolution to finer resolution, effects from clouds and topography must be considered (Dubayah and Loechel, 1997). Here the topographic correction was conducted on the base of NARR SW radiation already corrected for cloudiness effects (after procedure **C)**, as shown in Figure 4). The topographic solar radiation model and the technique for topographic correction we referred in this study, was developed originally by Dozier (1980) and Dozier and Frew (1990) assuming that the simulated total incoming radiation is at the sea level. Thus the original model performs an elevation correction before applying the topographic correction to solar radiation. However, the NARR incoming shortwave radiation is already at the NARR terrain elevation, thus we did not conduct the elevation correction in our implementation of the methodology. Even though there are elevation differences between the NARR terrain elevation at coarse resolution and the digital elevation model (DEM) at 1km resolution, we assume that the elevation effects caused by this difference are negligible compared to the topographic effects caused by the terrain complexity, such as blocking the incoming radiation by nearby terrain or reflecting radiation to surrounding terrain, especially in regions such as the Southern Appalachian mountains. The theoretical basis of the topographic radiation correction is briefly described as follows.

The total incoming solar radiation at a slope includes three components, namely the diffuse irradiance from the sky, direct irradiance from the Sun, and diffuse and direct irradiance from

366 nearby terrain (Dubayah and Paul, 1995). The total downward shortwave radiation can be
367 expressed as,

$$SW\downarrow_{tot}(i,j) = F\downarrow(i,j)V_d(i,j) + \delta\cos\theta_{i,j}\,B\downarrow(i,j) + C_t(i,j)F\uparrow(i,j) \qquad (9)$$

368 where $F\downarrow(i,j)$ is the diffuse irradiance, $F\uparrow(i,j)$ is the upwelling (terrain reflected) flux, and
369 $B\downarrow(i,j)$ is the direct beam irradiance; $V_d(i,j)$ is a sky view factor, $C_t(i,j)$ is a terrain
370 configuration factor; δ is a binary shadowing mask set equal to either 1 or 0 which means that
371 the point is in the shadow caused by nearby terrain blocking the Sun (cast-shadowing); $cos\theta_{i,j}$ is
372 the cosine of the local solar illumination angle indicating that if the Sun is below or above the
373 local horizon caused by the slope itself (self-shadowing), calculated as $cos\theta_{i,j} = cos\theta_0 cosS +$
374 $sin\theta_0 sinScos(\phi_0 - A)$, where $\theta_0$is solar zenith angle and $\phi_0$is solar azimuth angle, *S* and *A* are
375 slope magnitude and aspect. However, the original algorithm performs the topographic
376 correction based on the exo-atmospheric radiation after atmospheric attenuation noted as *I*
377 shown in Figure 7, whereas NARR estimates shortwave radiation at the surface, thus already
378 accounting for the solar illumination angle on the basis of its terrain. Therefore, we defined a
379 scaled cosine of solar illumination angle $\cos\theta^S$ which is calculated by the ratio of the cosine of
380 solar illumination angle based on DEM to that based on NARR terrain, to account for the
381 topographic difference between the DEM and NARR terrain, and used it in the IPW to illustrate
382 the topographic adjustment affecting the direct beam irradianceB ↓, as shown in Figure 7.

383 The first term in equation (9) is the diffuse irradiance from the sky, the second term in the
384 equation is the direct irradiance, and the last term is the irradiance reflected by nearby terrain. In
385 order to perform the topographic correction, the cloudiness corrected NARR hourly total
386 incoming shortwave radiation has to be partitioned into direct and diffuse components using the

atmospheric transmittance at shortwave derived from SRB-GICP radiation at surface and at the TOA, to obtain the direct beam irradiance $B\downarrow(i,j)$ and diffuse irradiance$F\downarrow(i,j)$. The partition is very important in the topographically complex region because the diffuse and direct radiation is affected by the terrain in different ways. The reflected radiation (upwelling) $F\uparrow(i,j)$ from the surrounding terrain then can be expressed as,

$$F\uparrow(i,j) = r(i,j)\left[F\downarrow(i,j)\left(1-V_d(i,j)\right)+\cos\theta_o\, B\downarrow(i,j)\right] \tag{10}$$

where the $r(i,j)$ is the surface reflectance (albedo). The sky view factor V_d varies from 1 (unobstructed) to 0 (completely obstructed), measuring the received diffuse irradiance at a local slope to that at an unobstructed slope, and can be expressed as,

$$V_d = \frac{1}{2\pi}\int_0^{2\pi}\left[cosSsin^2H_\phi + sinScos(\phi - A)\times(H_\phi - sinH_\phi cosH_\phi)\right]d\phi \tag{11}$$

where *S* and *A* are slope magnitude and aspect, and H_ϕ is the zenith angle to the local horizon in view direction ϕ. Note the notation (i,j) is neglected in equation (11), but each variable in this equation is at pixel base. The sky view factor V_d is large at an open area, but is small in the bottom of a narrow valley where partial sky is obstructed.

The terrain configuration factor $C_t(i,j)$ estimates the fraction of the surrounding terrain visible to the point varying from 0 (only sky visible) to 1 (only terrain visible), is calculated as,

$$C_t \approx \frac{1+\cos S}{2} - V_d \tag{12}$$

Thus, the $C_t(i,j)F\uparrow(i,j)$ is the radiation reflected by the surrounding visible terrain to the point(i,j), i.e. can be received at this point. Generally, the smaller the terrain configuration

403 factor is, the larger the sky view factor is. These auxiliary parameters, including V_d and C_t can be
404 calculated though Image Processing Workbench (IPW) (Frew, 1990) based on high-resolution
405 elevation data. Detailed description about the original methodology can be found in the study of
406 Dubayah and Paul (1995) and Dubayah and Loechel (1997).

407 **3.1 RESULTS AND EVALUATION**

408 **3.2 ELEVATION CORRECTION AND WIND ADJUSTMENT**

409 The results of the adjusted and the original NARR atmospheric temperature, atmospheric
410 pressure, specific humidity, downward longwave radiation and wind speed are shown in Figure 8
411 to Figure 13, demonstrating the seasonal and diurnal characteristics. The NLDAS2 fields are also
412 shown in the figures for reference. As can be seen from the figures, the adjusted fields
413 demonstrate very large spatial variability compared with the original fields, especially over
414 mountainous terrain. The largest variability is found in atmospheric pressure and in the southern
415 Appalachian Mountains, demonstrating very large contrast between the ridge lines and the
416 valleys. NLDAS2 forcing fields were corrected for the elevation effects based on its own
417 topographic terrain, thus also show little variability and topographic pattern. But the adjusted
418 NARR fields based on the 1km DEM illustrate much larger variability, clearly demonstrating the
419 effects of topography. Generally, at high elevation such as ridge lines in the Pigeon River Basin,
420 the atmospheric temperature, the atmospheric pressure, the specific humidity and the downward
421 longwave radiation are much smaller than that in the valleys. The difference magnitudes depend
422 on the seasonal and diurnal changes of the variables. For instance, the adjusted atmospheric
423 temperature is much different than the original NARR in the winter in contrast to that in the
424 summer, which is illustrated by the dark brown area in mountains (bottom panel) in the Mar.1

and Dec.1 in Figure 8. Other fields experience similar changes as atmospheric temperature, except for friction velocity and wind speed. Figure 12 and Figure 13 show the spatial friction velocity and wind speed at different times on different days in March, June, September and December. Unlike other atmospheric forcing fields, the spatial variability in friction velocity and wind speed primarily is dominated by landcover type, i.e. surface roughness length and displacement height. Although, the adjusted friction velocity accounting for land surface heterogeneity by variant surface roughness length shows slightly larger values than the raw friction velocity (Figure 12), the adjusted wind speed mainly shows smaller values than the raw NARR data due to the introduction of landcover-dependent displacement height illustrated by large blue areas in the bottom panel in Figure 13. The largest difference between both the friction velocity and wind speed before and after adjustment is in urban areas, where the roughness length is large (about 2.5 meters).

An intercomparison of these atmospheric forcing fields at AmeriFlux towers and at the Duke Environmental Physics Laboratory (DKEPL) tower (Table 1), including the raw NARR, adjusted NARR as well as the NLDAS2 forcing data, against tower observations are given in Figure 14 to Figure 19. Overall, the adjusted NARR fields demonstrate very good agreement with tower observations, generally showing better or at least as good as the raw NARR without adjustment. For instance, the adjusted atmospheric pressure at DKEPL tower, which is the only high-elevation flux-tower in the Appalachians shows very good performance as shown in Figure 15, while the raw NARR atmospheric pressure shows significant overestimation. The differences for other towers are not very large because of the small elevation difference the correction method accounts for as shown in Table 1. That is, towers are located at low elevations away from complex topography. Figure 18 shows that, the raw friction velocity of NARR is underestimated

448 at tower USChR, USDk2 and USDk3 where the adjusted friction velocity shows improved
449 estimates especially in the large friction velocity range. At USDk1 and DKEPL, both the original
450 and adjusted NARR data underestimate the friction velocity slightly. The adjusted wind speed
451 generally show much better performance than the raw NARR data which significantly
452 overestimates wind speed at all towers, as shown in Figure 19.

453 Figure 20 to Figure 24 show the probability density function (PDF) of these adjusted
454 atmospheric forcing fields for four physiographic provinces (as shown in Figure 1) and for the
455 four seasons. As it can be seen from Figure 20, the shape of PDFs of atmospheric temperature is
456 very similar for all seasons except in the summer (JJA), when it shows much less variability
457 illustrating much uniform atmospheric temperature distribution over the region in the summer.
458 The Appalachian Plateaus and the Blue Ridge have slightly smaller mean temperature than other
459 physiographic provinces, due to the cold temperatures in the mountainous region. The Coastal
460 plain always shows the largest mean temperature. The PDFs of atmospheric pressure show very
461 different shapes according to different physiographic provinces, while the dependence on
462 seasons is not very obvious, as shown in Figure 21. The PDFS for the Piedmont, interior low
463 plateaus and the coastal plain are very similar, with very little variability in atmospheric pressure.
464 The Blue Ridge, Valley and Ridge, and the Appalachian plateaus share a similar PDF shape, but
465 the changes are different. The Blue Ridge region exhibits the largest variability independently on
466 seasons. In another words, surface atmospheric pressure is not characterized by a marked
467 seasonal cycle. The PDFs of specific humidity are shown in Figure 22, which show very
468 difference behaviors both among seasons and among physiographic provinces. The similarity
469 among PDFs of different physiographic provinces within the same season is much larger than the
470 similarity between the PDFs of different seasons for a same physiographic province, which

implies that the temporal variability is much larger than the spatial variability. The PDFs of the downward longwave radiation are shown in Figure 23. As it can be seen, the mean downward longwave radiation for the Blue Ridge is always the lowest among the four physiographic provinces no matter the season. The Piedmont and Coastal plain have two peaks in the PDFs in DJF and SON, which is associated with the large diurnal variability corresponding to a daytime and a nighttime peak. The PDFs of wind speed demonstrate very similar shapes for all the physiographic provinces and seasons, as shown in Figure 24. The spatial variability of wind speed is significantly affected by landcover and also topography.

3.3 Topographically and Cloudiness Corrected Shortwave Radiation

The cloudiness and topographic corrections were dynamically applied to the regional radiation at hourly scale, with aid of auxiliary parameters as stated in Section 2.3. The time-invariant auxiliary input data include the sky view factor and the terrain configuration factor, both of which can be calculated from the DEM. The sky view factor represents the ratio of diffuse irradiance received at a particular slope to that at a completely unobstructed slope. The diffuse irradiance is blocked by nearby terrain, i.e. partially unobstructed sky view. Thus, a slope with larger sky view factor can receive more diffuse radiation than that with smaller sky view factor, for instance the bottom of a narrow valley. The terrain configuration factor then is a counterpart of the sky view factor, measuring the visible terrain to a slope. This factor is applied to the upwelling shortwave radiation, i.e. the reflected radiation from surrounding terrain, to account for the contribution of reflected radiation from the topography. Generally, the smaller the sky view factor, the larger the terrain configuration factor. The time-variant auxiliary input parameters include shortwave transmittance, surface albedo and the cosine of the local illumination angle. Transmittance directly represents atmospheric cloudy conditions,

494 significantly influencing the direct and diffuse radiation partitioning which is very important for
495 topographically complex regions. Albedo influences the reflected radiation from surrounding
496 terrain. The local illumination angle mainly affects the direct radiation received at a slope. The
497 albedo shows large spatial variability depending on land cover type (i.e. forest, cropland or bare
498 ground) and hydrometeorological conditions (dry/wet). The albedo diurnal cycle reflects mainly
499 the diurnal solar cycle, through the fraction of diffuse skylight. The cosine of the local
500 illumination angle shows large spatial variability in regions of complex terrain, due to the
501 relative position of the Sun and local slope. Besides topography, the diurnal variability and
502 seasonal variability in the local illumination angle are caused by the altitude and azimuth of the
503 Sun. As stated in Section 2.3, a scaled cosine of solar illumination angle was used in this study
504 to account for the topographic difference between the DEM and NARR terrain, since NARR
505 already accounts for the solar illumination angle on the basis of its own terrain at coarse scale.

506 Figure 25 and Figure 26 show the intermediate results performing the cloudiness and
507 topographic correction for a cloudy case and a clear case, respectively. In Figure 25, both the
508 direct and the total radiation components show very large variability due to cloud cover. In
509 Figure 26, all the radiation data show very uniform distribution, except for a cloud band in the
510 southwest corner, illustrated as the green bands in (e) and (h). The cosine of solar illumination
511 angle mainly affects the direct radiation component. Thus, when it is cloudy (Figure 25) and the
512 direct radiation component is very small (e), especially in the mountains where the illumination
513 effects are large. Therefore in the final resultant radiation after cloudiness and topographic
514 correction (g), the topographic effects are not very obvious. In other words, the cloudiness
515 correction dominates the radiation variability for a cloudy and partial cloudy case. On the
516 contrary, for a clear-sky case (Figure 26), the topographic effects are very clear in the

517 mountainous region, demonstrating complex spatial variability in the Southern Appalachians as
518 shown in (h) and (g), and thus the topographic corrections dominate the spatial variability in the
519 total shortwave radiation.

520 The comparison of the downward shortwave radiation between the NARR total incoming
521 SW radiation before and after corrections, the NLDAS2 field, as well as the SRB-GCIP solar
522 radiation for both the cloudy and clear case are shown in Figure 27 and Figure 28. Figure 27
523 shows the final radiation results (e) after both cloudiness and topographic corrections with very
524 good agreement when compared against the SRB-GCIP data and GOES imagery in terms of
525 cloudiness pattern in contrast with NLDAS2. In Figure 28, the final radiation result (e) maintains
526 the radiation magnitude as well as it incorporates the small cloudy band in the southwest corner,
527 meanwhile exhibiting large topographic variability.

528 The results of the downscaled shortwave radiation accounting for both cloudy effects and
529 topographic effects, the original NARR shortwave radiation, as well as the NLDAS2 shortwave
530 radiation, are shown in Figure 29 to illustrate seasonal and diurnal characteristics. As it can be
531 seen in the figure, at any given time the difference between the radiation before and after
532 corrections can be as large as about 550W/m^2 (e.g. the example shown for a day in September).
533 The topographic effects are more obvious in winter and in the early morning or late afternoon,
534 showing large variability in the mountains. Nevertheless, the dominant overall effect is due to the
535 cloudiness correction. The validation of the shortwave radiation before and after corrections, as
536 well as the NLDAS2 data at AmeriFlux towers against the tower observations are given in
537 Figure 30. Generally, both the NARR and NLDAS2 fields overestimate the incoming shortwave
538 radiation compared to the tower observations. The SRB-GCIP data underestimate the radiation a
539 little bit, due to its large spatial resolution. The corrected shortwave radiation compares well

against all tower observations (e.g. note lowest RMSE). Figure 31 provides the multiple-year averaged monthly mean diurnal cycle of shortwave radiation for the four datasets. The adjusted shortwave radiation data show a very good match with the observation in terms of the diurnal cycle shape as well as the peak times and peak values.

3. Summary and Discussion

Atmospheric forcing datasets at high resolution (1km×1km, hourly) including air temperature, air pressure, wind velocity, specific humidity, downward shortwave and longwave radiation were developed for the IPHEx-H4SE project based on the North American Regional Reanalysis (NARR) products originally at 32-km spatial resolution and 3-hour temporal resolution, for a five-year period (2007-2011) over the Southeast US. Specific downscaling methods in complex terrain region require elevation correction to the coarse resolution atmospheric forcing fields. An elevation correction was applied to the NARR air temperature, air pressure, specific humidity and downward longwave radiation using dynamic lapse rates derived from atmospheric temperature profiles. Friction velocity was adjusted based on a relationship between the geostrophic drag coefficients and the Rossby Number, and then was used to recalculate wind velocity. The downward shortwave radiation data were first temporally interpolated to hourly using a temporal interpolation method based on the solar zenith angle as well as the diurnal cycle of NARR cloudiness. Then the real-time cloudiness pattern were derived from the SRB-GCIP dataset, and were applied to correct cloudy effects for NARR shortwave radiation, by matching the spatial PDF of NARR data the that of the SRB-GCIP data. The topographic effects then were corrected based on a topographic solar radiation model. The adjusted atmospheric forcing

562 datasets demonstrate larger spatial variability compared to the raw NARR fields, especially in
563 mountainous regions. The comparison between the atmospheric forcing data against observations
564 at AmeriFlux towers and the DKEPL tower reveals that the adjustments to the NARR fields
565 improve these atmospheric variables, especially in the mountainous regions where large
566 elevation differences exist between the NARR terrain and local DEM. All datasets are available
567 at the website of IPHEx (http://iphex.pratt.duke.edu/), and be open-access to the PMM science
568 team and all H4SE participants.

569

References

Berg, A.A., Famiglietti, J.S., Walker, J.P., Houser, P.R., 2003. Impact of bias correction to reanalysis products on simulations of North American soil moisture and hydrological fluxes. Journal of Geophysical Research-Atmospheres, 108(D16).

Chavez, P.S., 1996. Image-based atmospheric corrections revisited and improved. Photogrammetric Engineering and Remote Sensing, 62(9).

Cosgrove, B.A. et al., 2003. Real-time and retrospective forcing in the North American Land Data Assimilation System (NLDAS) project. Journal of Geophysical Research-Atmospheres, 108(D22).

Dozier, J., 1980. A clear-sky spectral solar radiation model for snow-covered mountainous terrain. Water Resources Research, 16(4): 709-718.

Dozier, J., Frew, J., 1990. Rapid calculation of terrain parameters for radiation modeling fromdigital elevation data. IEEE Thransactions on Geoscience and Remote Sensing, 28(5): 963-969.

Dubayah, R., Dozier, J., Davis, F.W., 1990. Topographic distribution of clear-sky radiation over the Konza Prairie, Kansas. Water Resources Research, 26(4): 679-690.

Dubayah, R., Loechel, S., 1997. Modeling topographic solar radiation using GOES data. Journal of Applied Meteorology, 36: 141-154.

Dubayah, R., Paul, M., 1995. Topographic solar radiation models for GIS. International Journal of Geographical Information Systems, 9(4): 405-419.

590 Frew, J.E.J., 1990. The Image Processing Workbench, UNIVERSITY OF CALIFORNIA, Santa
591 Barbara. [Doctor].

592 Gao, L., Bernhardt, M., Schulz, K., 2012. Elevation correction of ERA-Interim temperature data
593 in complex terrain. Hydrol Earth Syst Sc, 16(12): 4661-4673.

594 Lenters, J.D., Coe, M.T., Foley, J.A., 2000. Surface water balance of the continental United
595 States, 1963-1995: Regional evaluation of a terrestrial biosphere model and the
596 NCEP/NCAR reanalysis. Journal of Geophysical Research-Atmospheres, 105(D17):
597 22393-22425.

598 Lettau, H.H., 1959. Wind profile, surface stress and geostrophic drag coefficients in the
599 atmospheric surface layer. Advances in geophysics, 6: 241.

600 Mesinger, F. et al., 2006. North American regional reanalysis. Bulletin of the American
601 Meteorological Society, 87(3): 343-360.

602 Mitchell, K.E. et al., 2004. The multi-institution North American Land Data Assimilation System
603 (NLDAS): Utilizing multiple GCIP products and partners in a continental distributed
604 hydrological modeling system. Journal of Geophysical Research-Atmospheres, 109(D7).

605 Pinker, R.T. et al., 2003. Surface radiation budgets in support of the GEWEX Continental-Scale
606 International Project (GCIP) and the GEWEX Americas Prediction Project (GAPP),
607 including the North American Land Data Assimilation System (NLDAS) Project. Journal
608 of Geophysical Research-Atmospheres, 108(D22).

609 Schaaf, C.B. et al., 2002. First operational BRDF, albedo nadir reflectance products from
610 MODIS. Remote Sens. Environ., 83(1-2): 135-148.

611 Schomburg, A., Venema, V., Lindau, R., Ament, F., Simmer, C., 2010. A downscaling scheme
612 for atmospheric variables to drive soil–vegetation–atmosphere transfer models. Tellus B,
613 62(4): 242-258.

614 Schroeder, T.A., Hember, R., Coops, N.C., Liang, S.L., 2009. Validation of Solar Radiation
615 Surfaces from MODIS and Reanalysis Data over Topographically Complex Terrain.
616 Journal of Applied Meteorology and Climatology, 48(12): 2441-2458.

617 Tao, J., Barros, A.P., 2013a. Coupled prediction of flood response and debris flow initiation
618 during warm and cold season events in the Southern Appalachians, USA. Hydrol. Earth
619 Syst. Sci. Discuss., 10(7): 8365-8419.

620 Tao, J., Barros, A.P., 2013b. Prospects for Flash Flood Forecasting in Mountainous Regions–An
621 Investigation of Tropical Storm Fay in the Southern Appalachians. J. Hydrol.

622 Xia, Y.L. et al., 2012a. Continental-scale water and energy flux analysis and validation for North
623 American Land Data Assimilation System project phase 2 (NLDAS-2): 2. Validation of
624 model-simulated streamflow. Journal of Geophysical Research-Atmospheres, 117.

625 Xia, Y.L. et al., 2012b. Continental-scale water and energy flux analysis and validation for the
626 North American Land Data Assimilation System project phase 2 (NLDAS-2): 1.
627 Intercomparison and application of model products. Journal of Geophysical Research-
628 Atmospheres, 117.

629 Yildiz, O., Barros, A.P., 2007. Elucidating vegetation controls on the hydroclimatology of a mid-
630 latitude basin. J. Hydrol., 333(2-4): 431-448.

631 Yildiz, O., Barros, A.P., 2009. Evaluating spatial variability and scale effects on hydrologic
632 processes in a midsize river basin. Scientific Research and Essays, 4(4): 217-225.

633

634

635 ## List of Tables

647

648 ## List of Figures

821

822 Table 1 - Landcover of the referred towers locations

Station	MODIS Landcover (IGBP)	MODIS Landcover (UMD Type)	Tower footprint
US-Akn	Mixed Forest	Mixed Forest	Forest
US-ChR	Deciduous Broad-leaf Forest	Deciduous Broad-leaf Forest	Chestnut ridge
US-Dk1	Mixed Forest	Woody Savannas	Grassland, open field
US-Dk2	Mixed Forest	Woody Savannas	Hardwoods
US-Dk3	Mixed Forest	Mixed Forest	Loblolly pine
US-WBW	Deciduous Broadleaf Forest	Deciduous Broadleaf Forest	Oak Ridge
DKEPL Tower	Mixed Forest	Mixed Forest	Forest

823

824 Table 2 – Statistics of atmospheric temperature (K) at 10m above ground for each physiographic
825 procinve and for four seasons.

Atmos.Temp.	App. Pla.	Val.&Rig.	Piedmont	Blue Ridge	Inter. Pla.	Coa. Plain	
Mean	275.8	276.5	278.8	275.4	276.0	281.5	DJF
Median	275.2	276.1	278.2	275.2	275.3	281.3	
Std.	6.6	6.7	6.5	6.7	6.4	**6.8**	
Max.X-axis	0.2	0.2	0.2	0.2	0.2	0.2	
Mean	287.1	287.5	289.2	285.5	287.8	290.9	MAM
Median	287.6	287.9	289.7	285.9	288.2	291.4	
Std.	6.9	7.0	6.9	6.7	**7.1**	6.6	
Max.X-axis	0.2	0.2	0.2	0.2	0.2	0.2	
Mean	297.5	297.9	300.2	295.6	298.5	300.9	JJA
Median	297.6	298.0	300.1	295.6	298.7	300.6	
Std.	3.9	**4.2**	4.1	4.0	3.9	3.9	
Max.X-axis	0.4	0.2	0.2	0.2	0.4	0.2	
Mean	288.2	288.6	290.3	286.6	288.7	291.8	SON
Median	288.4	288.8	290.6	287.0	288.9	292.6	
Std.	7.2	7.3	7.3	7.0	**7.4**	7.2	
Max.X-axis	0.2	0.2	0.2	0.2	0.1	0.2	

826

827

828 Table 3 – Statistics of atmospheric pressure (mb) at 10m above ground for each physiographic
829 province and for four seasons.

Atmos.Press.	App. Pla.	Val.&Rig.	Piedmont	Blue Ridge	Inter. Pla.	Coa. Plain	
Mean	961.7	965.2	991.9	927.2	984.1	1010.7	DJF
Median	962.6	971.9	992.9	928.6	985.0	1011.0	
Std.	17.6	25.8	12.5	**32.4**	10.4	8.5	
Max.X-axis	0.4	0.2	0.4	0.2	0.4	0.5	
Mean	960.3	963.8	989.8	927.4	981.6	1008.1	MAM
Median	961.1	970.3	990.7	928.9	982.4	1008.4	
Std.	16.7	24.5	12.1	**31.3**	9.7	8.2	
Max.X-axis	0.4	0.4	0.4	0.2	0.5	0.5	
Mean	960.3	963.5	988.2	928.4	981.0	1005.9	JJA
Median	961.3	970.2	989.2	929.6	981.6	1006.3	
Std.	15.5	23.1	10.5	**29.8**	8.1	6.4	
Max.X-axis	0.4	0.4	0.4	0.2	1.0	1.0	
Mean	961.8	965.2	990.9	928.9	983.2	1008.7	SON
Median	962.7	971.9	991.9	930.3	984.0	1009.0	
Std.	16.4	24.1	11.6	**31.0**	9.2	7.5	
Max.X-axis	0.4	0.4	0.4	0.2	0.5	0.5	

830

831

832

833 Table 4 – Statistics of specific humidity (g/kg) at 10m above ground for each physiographic
834 procinve and for four seasons.

Spec. Humid.	App. Pla.	Val.&Rig.	Piedmont	Blue Ridge	Inter. Pla.	Coa. Plain	
Mean	4.0	4.2	4.5	4.0	4.0	5.5	DJF
Median	3.3	3.4	3.6	3.2	3.4	4.7	
Std.	2.3	2.3	**2.6**	2.3	2.3	3.0	
Max.X-axis	0.2	0.2	0.2	0.2	0.2	0.1	
Mean	7.7	7.8	8.3	7.3	8.1	9.3	MAM
Median	7.5	7.6	8.1	7.2	7.8	9.4	
Std.	3.2	3.2	**3.5**	3.0	3.4	**3.5**	
Max.X-axis	0.1	0.1	0.1	0.1	0.1	0.1	
Mean	13.8	13.7	14.1	12.8	14.5	15.8	JJA
Median	13.9	13.8	14.4	12.9	14.7	16.0	
Std.	2.6	2.6	2.5	2.4	**2.8**	2.4	
Max.X-axis	0.1	0.1	0.1	0.1	0.1	0.1	
Mean	7.8	8.0	8.6	7.6	8.1	10.0	SON
Median	7.4	7.6	8.4	7.4	7.6	9.9	
Std.	3.4	3.4	3.7	3.3	3.5	**4.2**	
Max.X-axis	0.1	0.1	0.1	0.1	0.1	0.0	

835

836

837

838

839 Table 5 – Statistics of downward longwave radiation at surface (W/m^2) for each physiographic
840 procinve and for four seasons.

DLWR	App. Pla.	Val.&Rig.	Piedmont	Blue Ridge	Inter. Pla.	Coa. Plain	
Mean	272.0	274.0	278.0	258.6	276.2	291.3	DJF
Median	271.1	272.0	272.8	253.3	276.4	288.6	
Std.	51.1	52.1	54.5	53.1	51.3	**57.6**	
Max.X-axis	0.1	0.1	0.1	0.1	0.1	0.1	
Mean	321.2	322.8	330.6	304.9	327.4	341.2	MAM
Median	325.9	327.3	335.8	308.7	332.5	346.7	
Std.	47.5	49.0	52.0	48.7	48.2	**52.2**	
Max.X-axis	0.1	0.1	0.1	0.1	0.1	0.1	
Mean	387.5	391.1	410.0	369.2	395.8	424.3	JJA
Median	390.7	394.1	413.3	370.5	400.3	427.7	
Std.	35.2	**37.8**	35.7	35.6	35.5	31.7	
Max.X-axis	0.2	0.2	0.2	0.2	0.2	0.2	
Mean	324.3	326.5	338.9	309.1	329.7	351.8	SON
Median	328.0	329.9	346.5	311.2	334.1	362.5	
Std.	53.7	55.5	59.0	54.5	55.0	**60.3**	
Max.X-axis	0.1	0.1	0.1	0.1	0.1	0.1	

841

842

843 Table 6 – Statistics of wind speed (m/s) at 10m above ground for each physiographic procinve
844 and for four seasons.

WindSpeed	App. Pla.	Val.&Rig.	Piedmont	Blue Ridge	Inter. Pla.	Coa. Plain	
Mean	2.8	3.3	3.0	3.2	3.6	3.0	DJF
Median	2.4	2.8	2.7	2.8	3.0	2.7	
Std.	1.7	2.2	1.8	1.9	**2.3**	1.8	
Max.X-axis	0.2	0.2	0.2	0.2	0.1	0.2	
Mean	2.7	3.2	3.0	3.0	3.6	3.0	MAM
Median	2.3	2.7	2.7	2.6	3.0	2.6	
Std.	1.6	2.1	1.7	1.8	**2.3**	1.8	
Max.X-axis	0.2	0.2	0.2	0.2	0.1	0.2	
Mean	1.9	2.2	2.3	2.0	2.5	2.4	JJA
Median	1.7	1.9	2.1	1.8	2.1	2.2	
Std.	1.1	1.4	1.3	1.2	**1.5**	1.3	
Max.X-axis	0.2	0.2	0.2	0.2	0.2	0.2	
Mean	2.3	2.7	2.6	2.6	3.0	2.7	SON
Median	2.0	2.3	2.4	2.2	2.5	2.4	
Std.	1.4	1.8	1.6	1.6	**2.0**	1.6	
Max.X-axis	0.2	0.2	0.2	0.2	0.2	0.2	

845

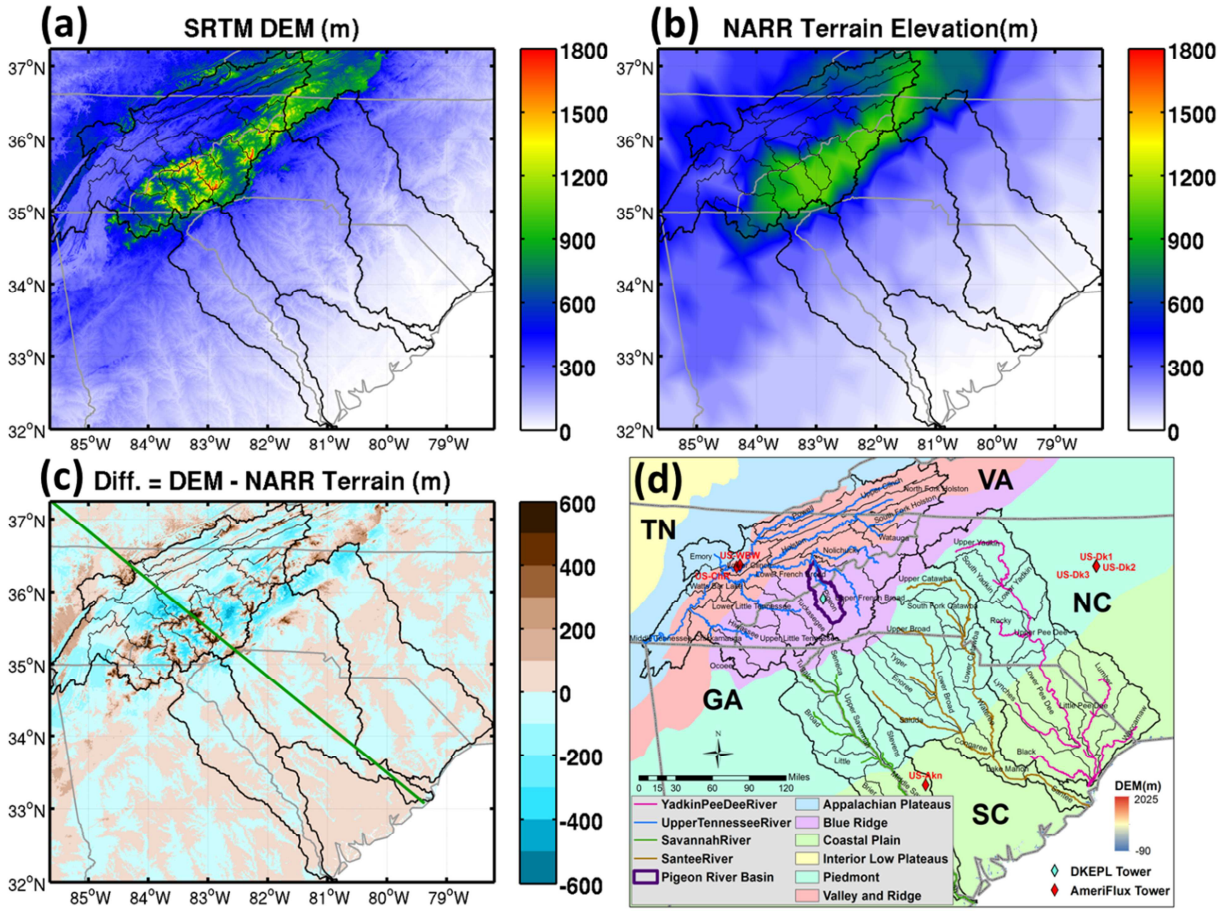

Figure 1 – The local 1km DEM data resampled from SRTM (a), the elevation data bi-linearly interpolated from NARR terrain at 32km (b), the elevation difference between the two (c), calculating from (a)-(b); A transect line crossing the northwest to the southeast of the area is shown in (c), is used to illustrate the elevation correction; the panel (d) shows the physiographic provinces, including Appalachian Plateaus, Valley and Ridge, Piedmont, Blue Ridge, Interior low plateaus and Coastal plain, generated from the Physical Divisions of the United States[3]. The locations of AmeriFlux towers and the tower from the Duke Environmental Physics Laboratory (DKEPL) are also shown in (d).

[3] http://water.usgs.gov/lookup/getspatial?physio

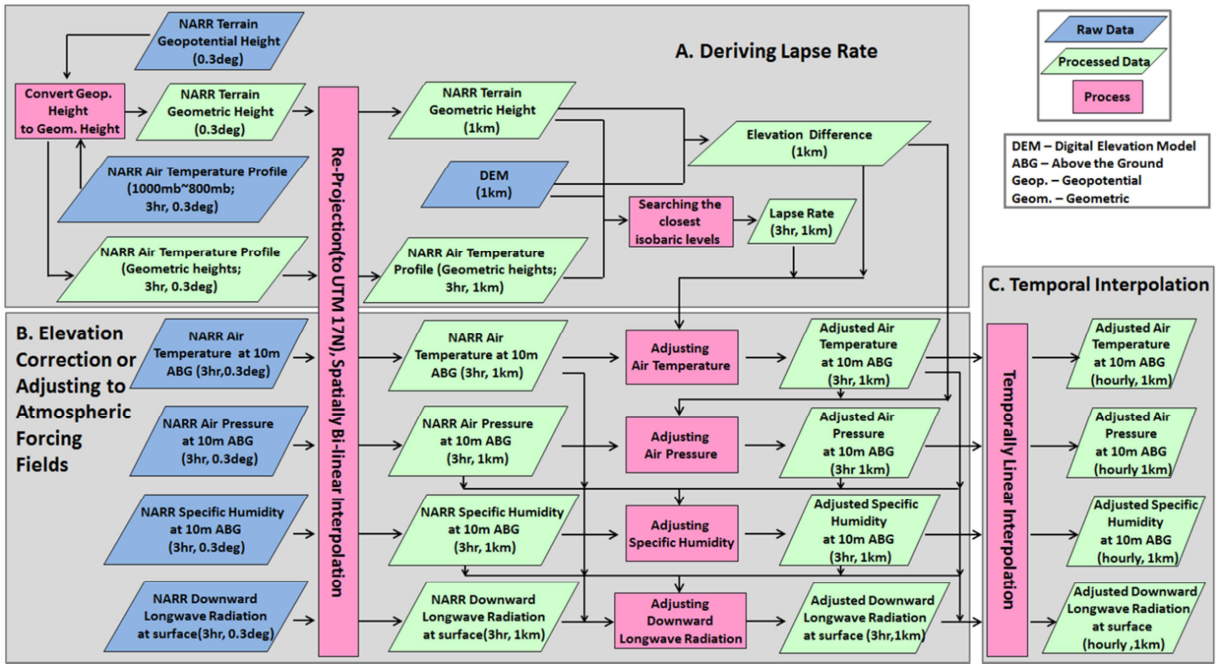

Figure 2 - Flowchart for elevation correction to NARR air temperature, air pressure, specific humidity and downward longwave radiation. The parallelogram with blue background represents the original raw data, with the green background representing the intermediate or processed results, the rectangle with pink background means processes.

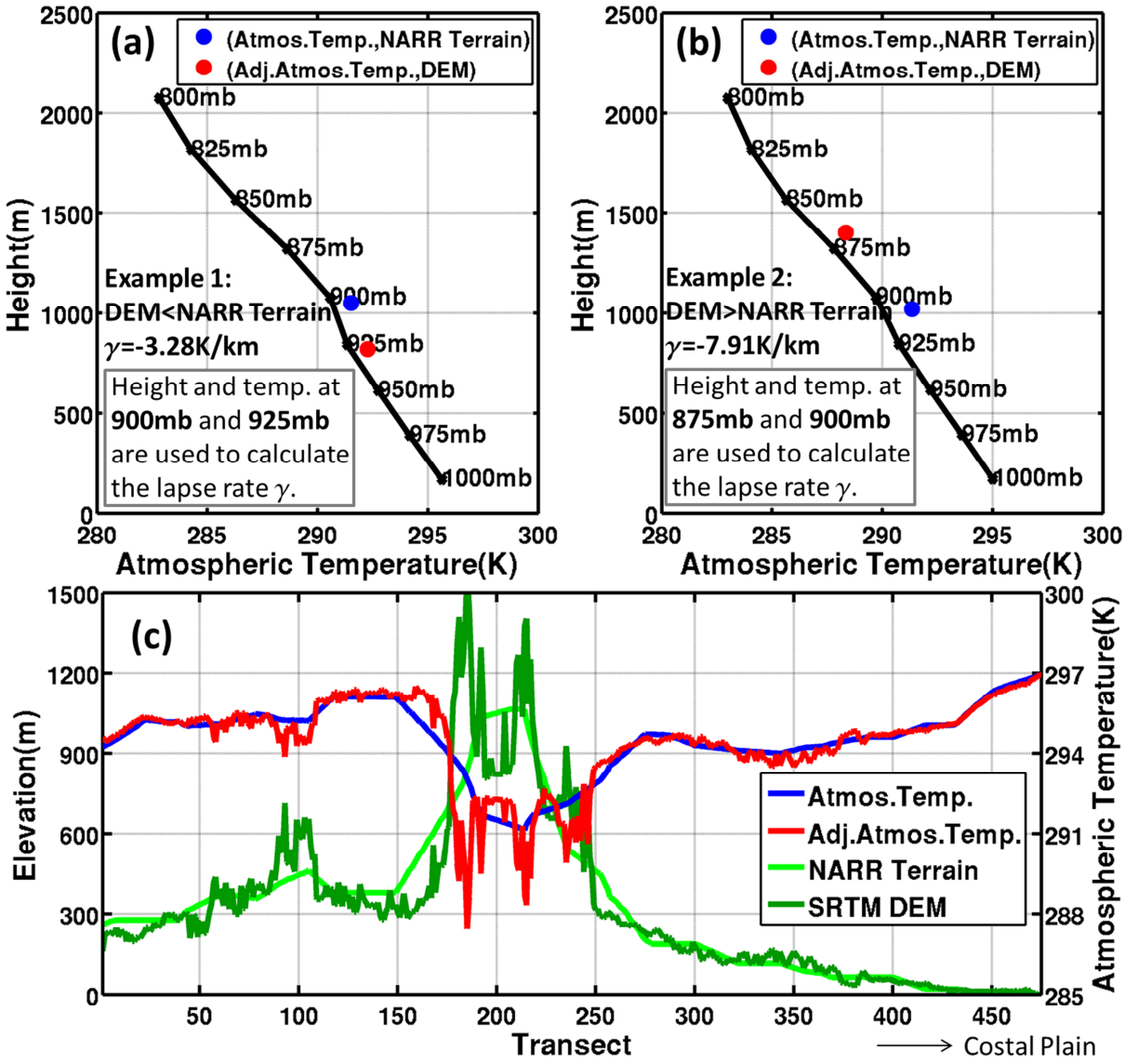

Figure 3 – Example of elevation correction to atmospheric temperature at 10m above ground (ABG) at a pixel where the DEM is less than the NARR terrain (a), and a pixel where the DEM is larger (b); the bottom panel (c) shows the elevation correction along the transect line as shown in Figure 1.

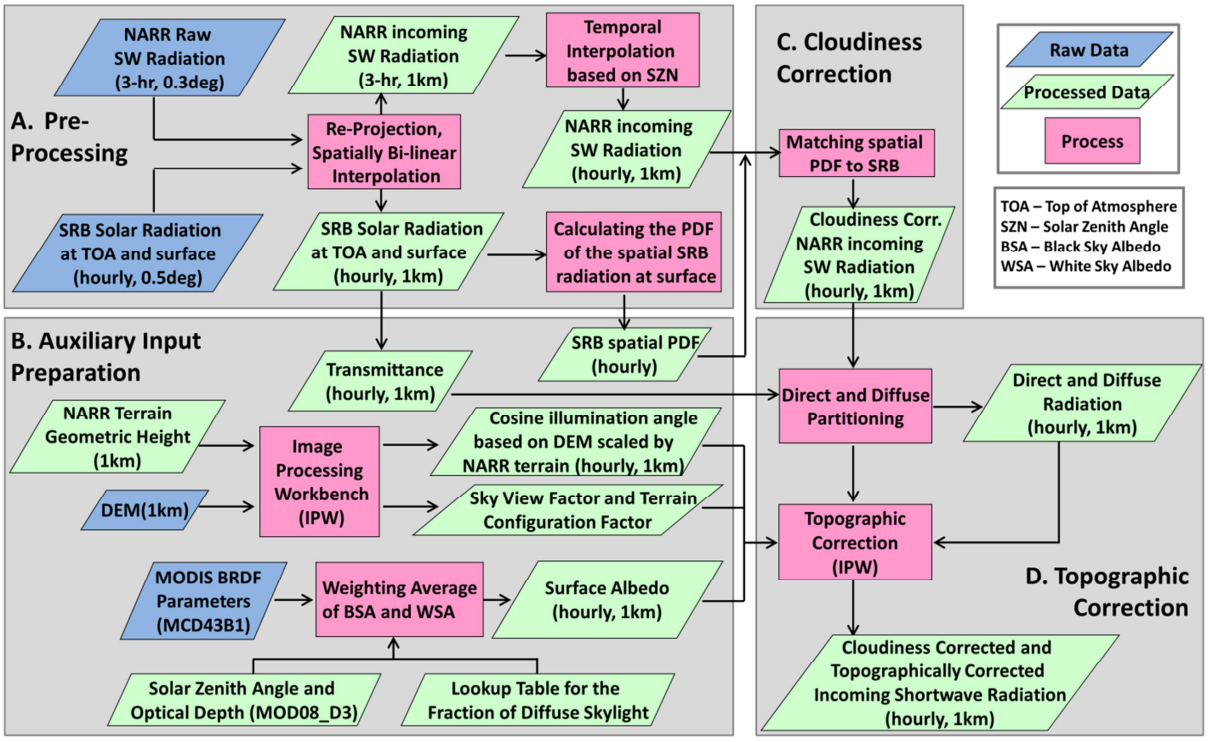

868

869 Figure 4 – The flowchart illustrating the procedures to generate the cloudiness-corrected and

870 topographically corrected hourly shortwave radiation data from NARR 3-hr shortwave radiation.

871

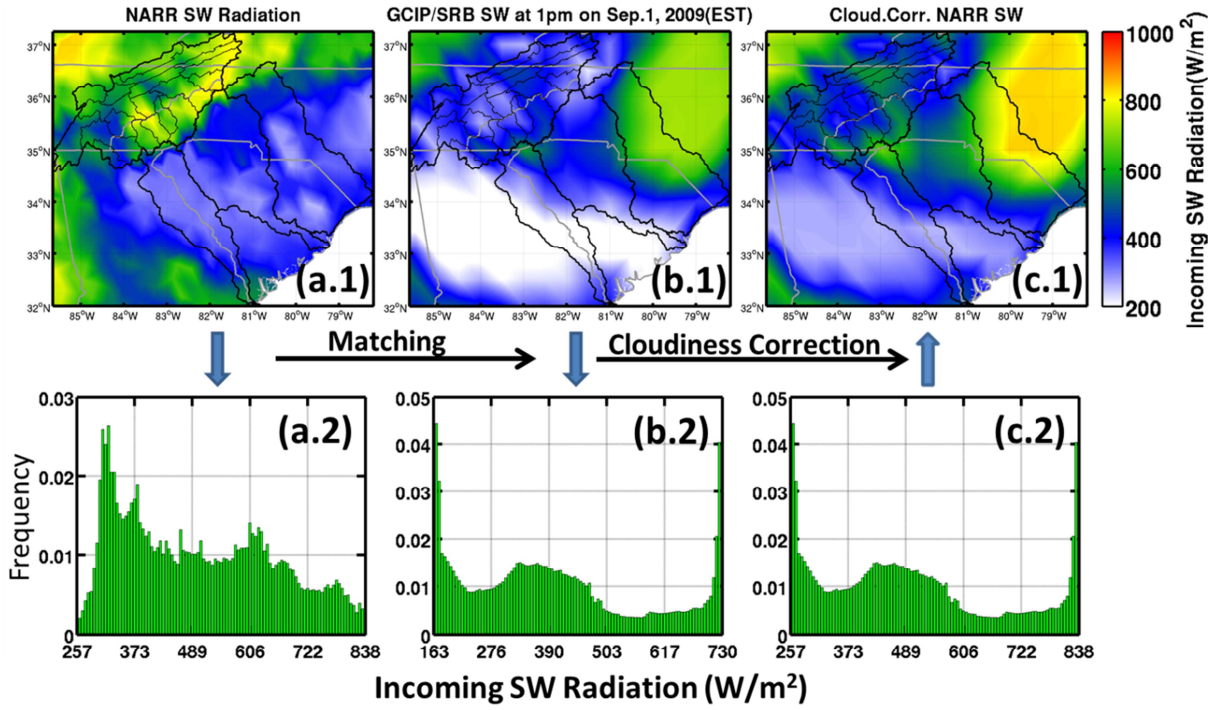

872

873 Figure 5 – The example of cloudiness correction to NARR SW radiation by matching the spatial
874 PDF to that of GCIP/SRB SW data over the SE US, illustrated by the data at 1pm (EST) on Sep.
875 1, 2009.

876

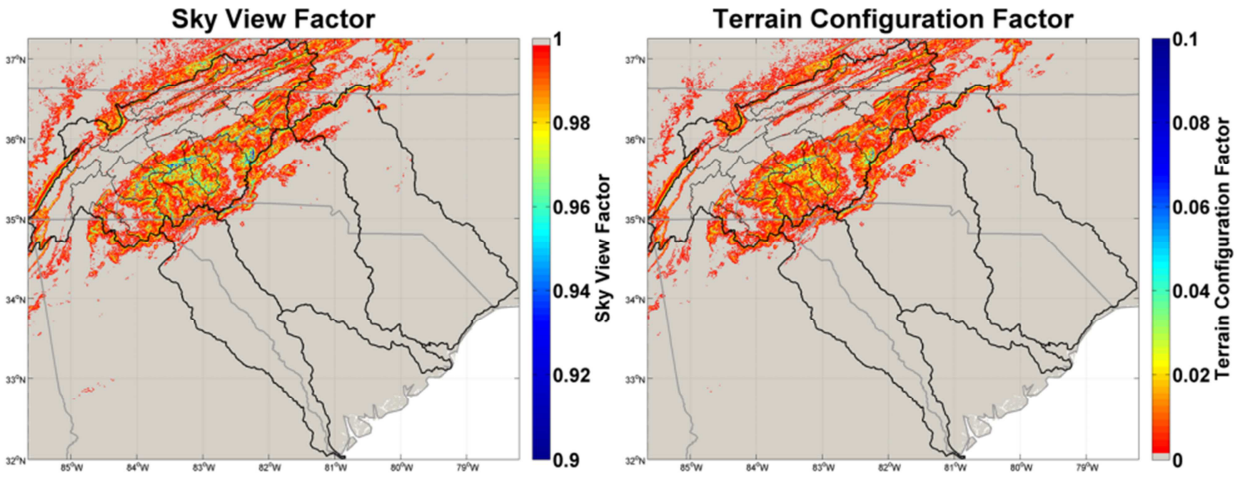

Figure 6 – The Fixed auxiliary input parameters for topographic radiation correction, including the sky view factor (left) and the terrain configuration factor (right).

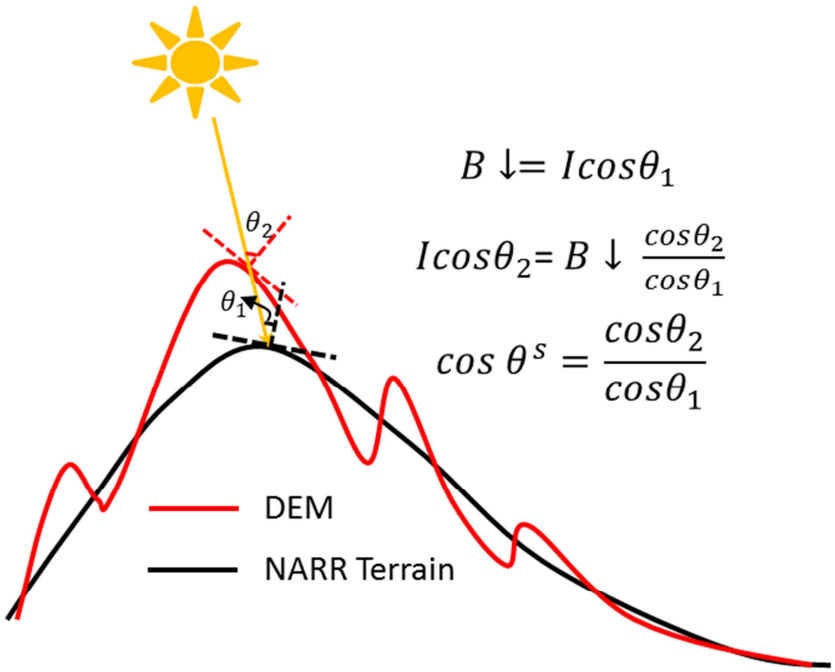

Figure 7 – The difference in the local solar illumination angle caused by the different topography of DEM and NARR terrain. **I** is the exoatmospheric radiation after atmospheric attenuation and arrives at the NARR terrain; the $\boldsymbol{\theta_1}$is the solar illumination angle based on NARR terrain, and the $\boldsymbol{\theta_2}$is the solar illumination angle based on DEM. The scaled cosine of solar illumination angle $\boldsymbol{cos\theta^S}$ is defined by the ratio of the cosine of solar illumination angle based on DEM to that based on NARR terrain to account for the topographic difference, and is used to illustrate the topographic effect acting on the direct beam irradiance **B**↓ in the IPW, instead of using $\boldsymbol{cos\theta_2}$directly.

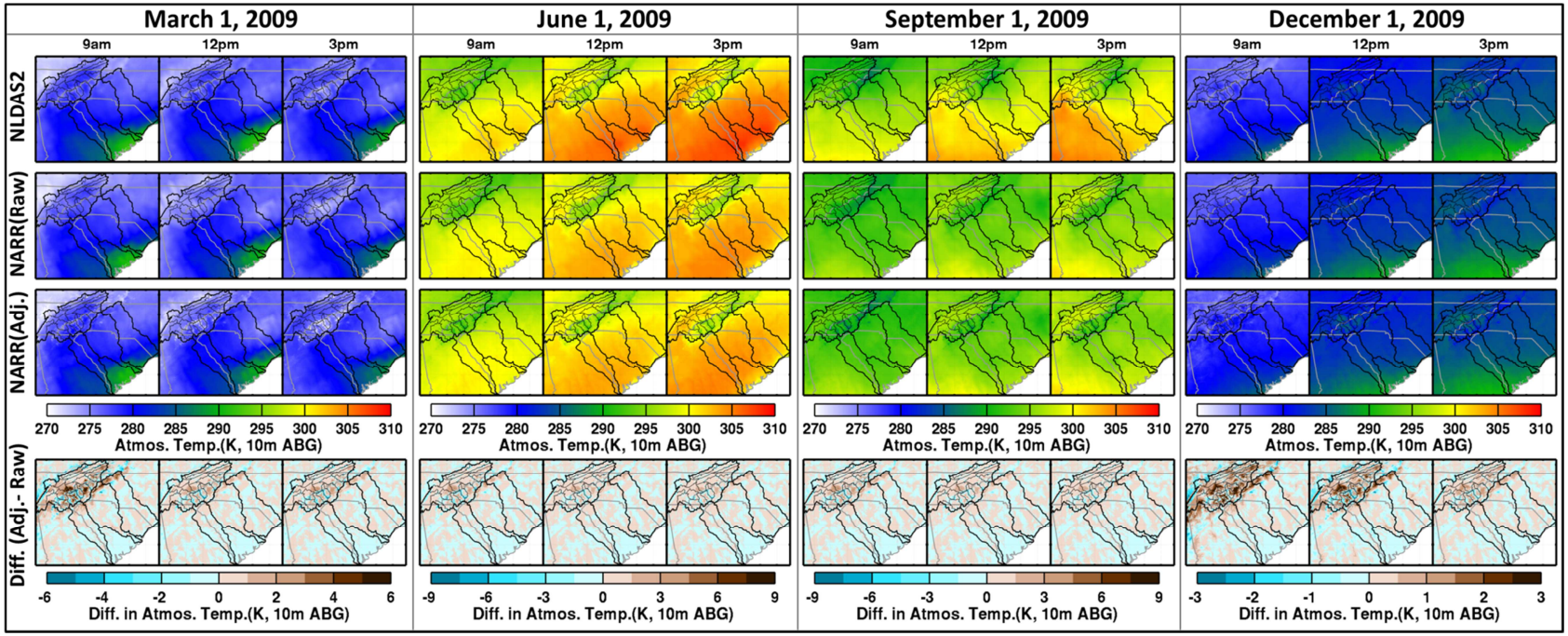

Figure 8 – The atmospheric temperature at 10m above ground over the SE US from NLDAS2, NARR before (Raw) and after (Adj) elevation correction/adjustment at 9am, noon and 3pm (EST) on Mar. 1, Jun. 1, Sep. 1, and Dec. 1 in 2009 from the left to the right, respectively. The bottom figures show the difference between the NARR atmospheric temperature after and before adjustment, using a symmetrical blue-brown color scale such that the brown color represents positive values and the blue color represent negative values.

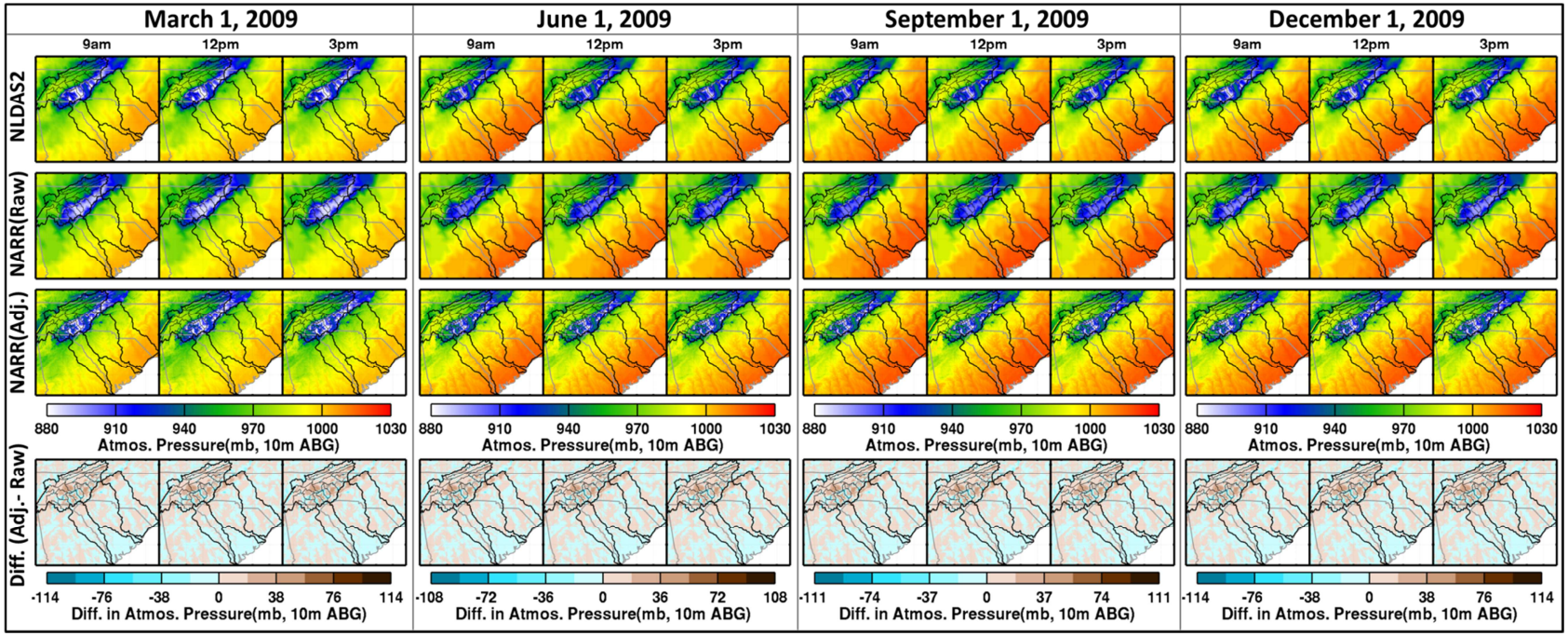

Figure 9 – The atmospheric pressure at 10m above ground over the SE US from NLDAS2, NARR before (Raw) and after (Adj) elevation correction/adjustment at 9am, noon and 3pm (EST) on Mar. 1, Jun. 1, Sep. 1, and Dec. 1 in 2009 from the left to the right, respectively. The bottom figures show the difference between the NARR atmospheric pressure after and before adjustment, using a symmetrical blue-brown color scale such that the brown color represents positive values and the blue color represent negative values.

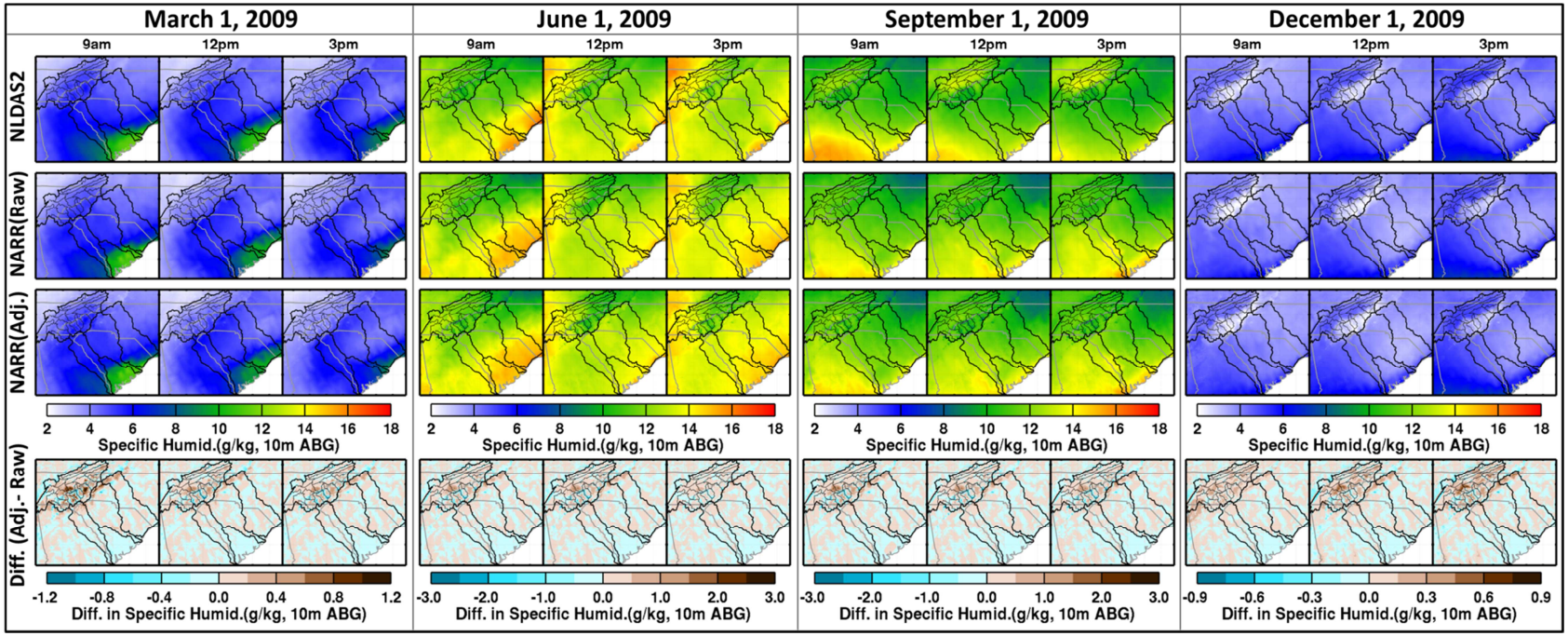

Figure 10 – The specific humidity at 10m above ground over the SE US from NLDAS2, NARR before (Raw) and after (Adj) elevation correction/adjustment at 9am, noon and 3pm (EST) on Mar. 1, Jun. 1, Sep. 1, and Dec. 1 in 2009 from the left to the right, respectively. The bottom figures show the difference between the NARR specific humidity after and before adjustment, using a symmetrical blue-brown color scale such that the brown color represents positive values and the blue color represent negative values.

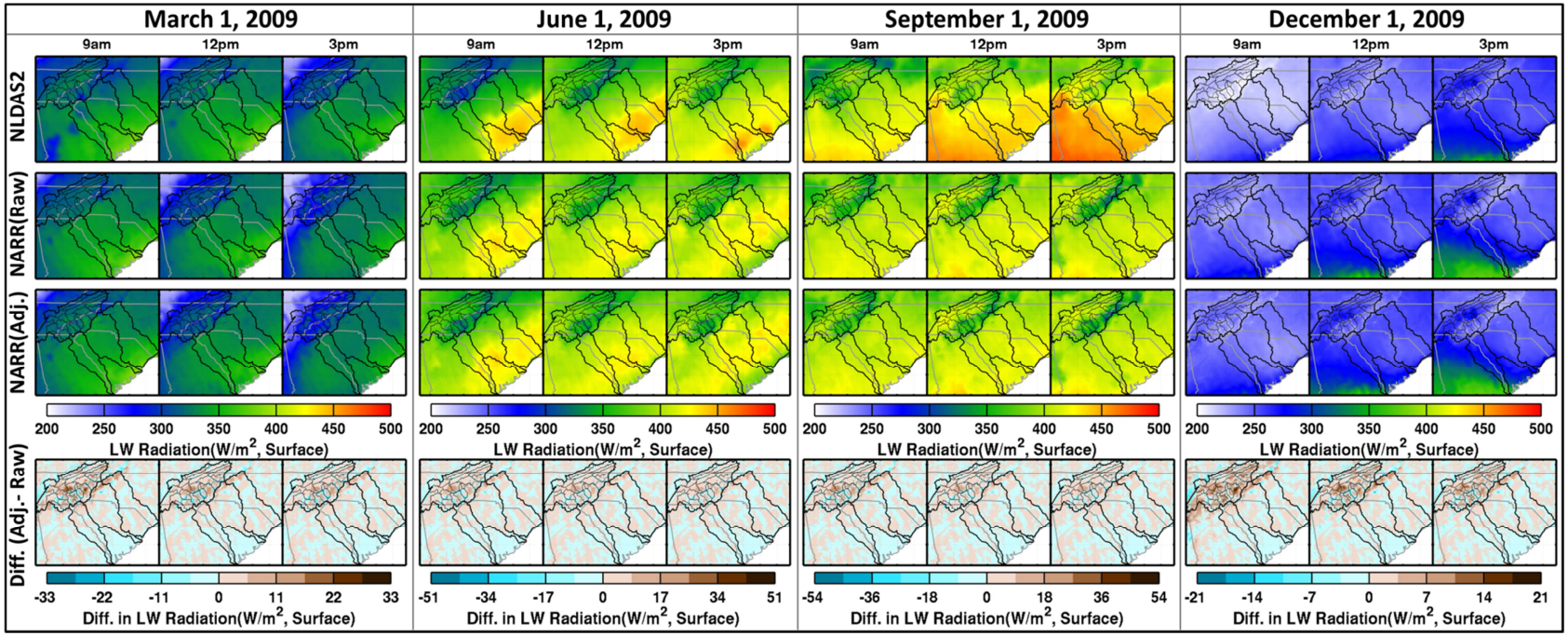

Figure 11 – The downward longwave radiation at surface over the SE US from NLDAS2, NARR before (Raw) and after (Adj) elevation correction/adjustment at 9am, noon and 3pm (EST) on Mar. 1, Jun. 1, Sep. 1, and Dec. 1 in 2009 from the left to the right, respectively. The bottom figures show the difference between the NARR downward longwave radiation after and before adjustment, using a symmetrical blue-brown color scale such that the brown color represents positive values and the blue color represent negative values.

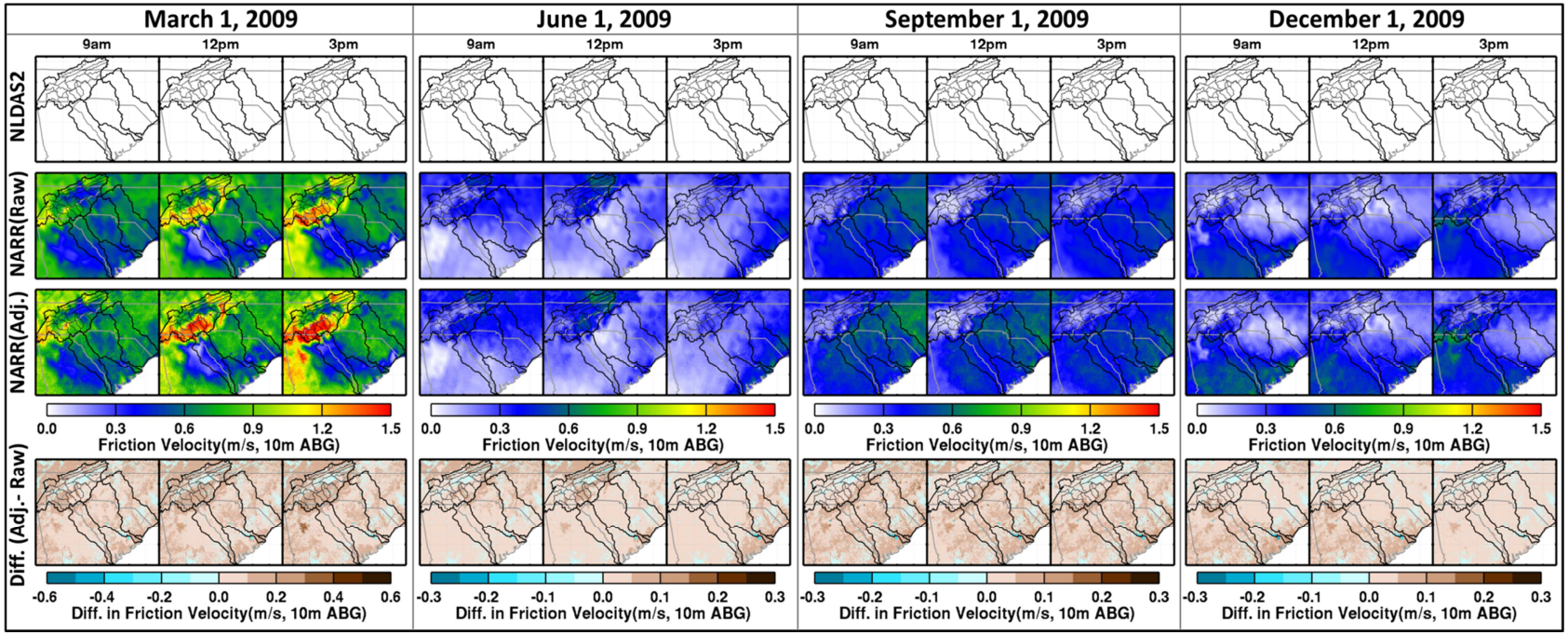

916

917 Figure 12 – The friction velocity near the surface over the SE US from NARR before (Raw) and after (Adj) elevation
918 correction/adjustment at 9am, noon and 3pm (EST) on Mar. 1, Jun. 1, Sep. 1, and Dec. 1 in 2009 from the left to the right, respectively.
919 The bottom figures show the difference between the NARR wind speed after and before adjustment, using a symmetrical blue-brown
920 color scale such that the brown color represents positive values and the blue color represent negative values.

921

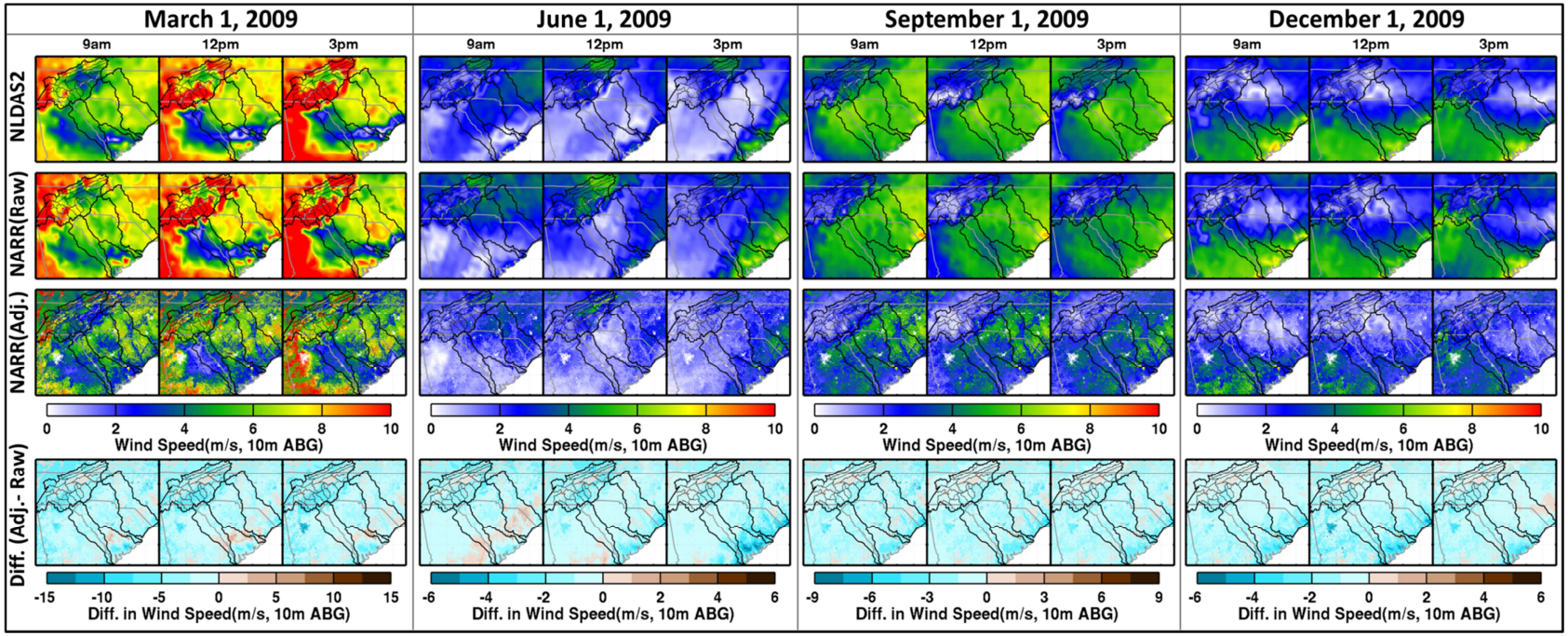

Figure 13 – The wind speed at 10m above ground over the SE US from NLDAS2, NARR before (Raw) and after (Adj) elevation correction/adjustment at 9am, noon and 3pm (EST) on Mar. 1, Jun. 1, Sep. 1, and Dec. 1 in 2009 from the left to the right, respectively. The bottom figures show the difference between the NARR wind speed after and before adjustment, using a symmetrical blue-brown color scale such that the brown color represents positive values and the blue color represent negative values.

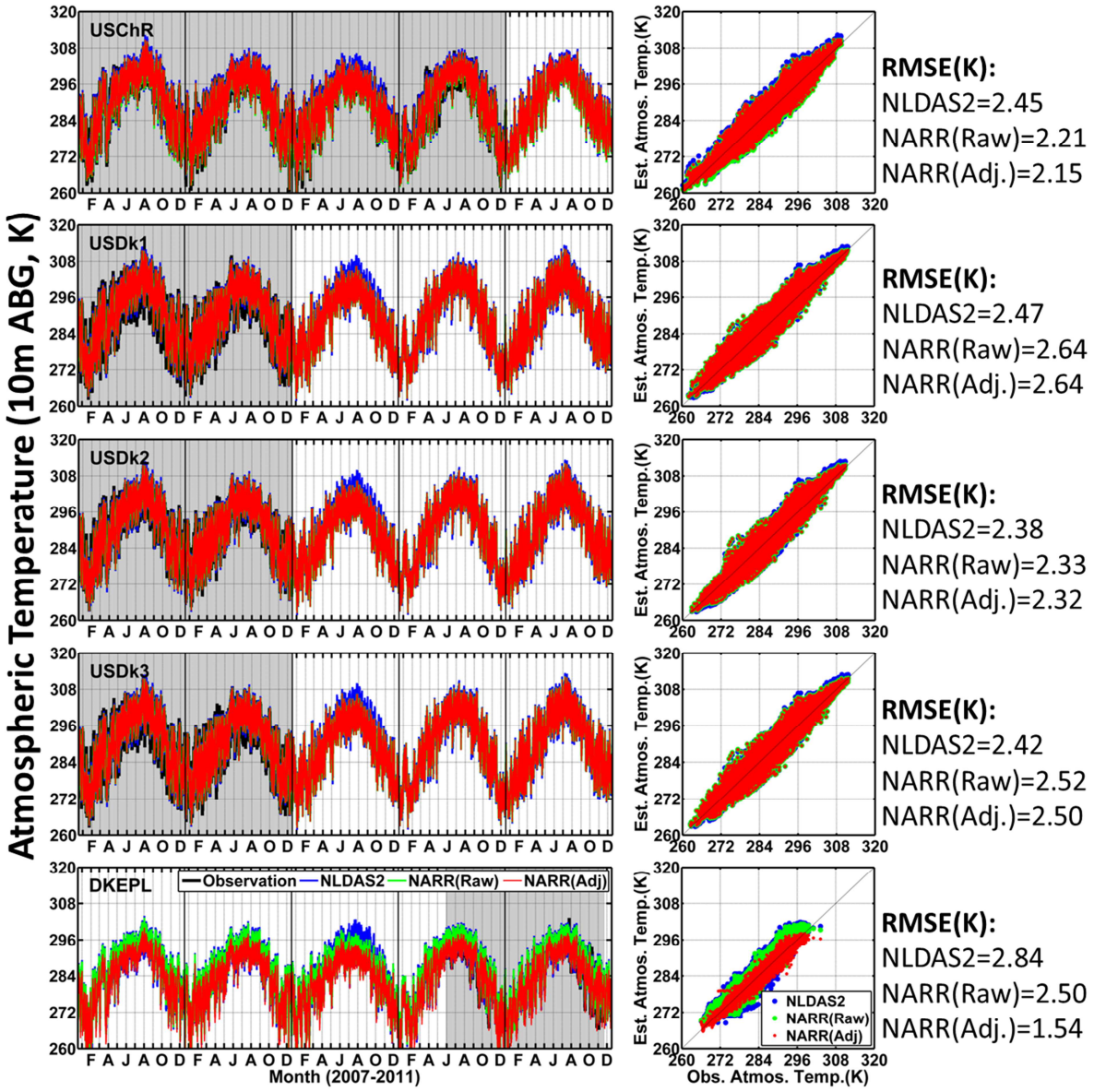

928

929 Figure 14 – The comparison between observed and estimated atmospheric temperature from
930 NLDAS2, NARR before (Raw) and after (Adj) elevation correction in the five year period, at
931 four Ameriflux towers, namely US-ChR, US-Dk1, US-Dk2, US-Dk3, and the DKEPL tower
932 from the top to the bottom, respectively. The shaded windows represent the observation
933 available period.

934

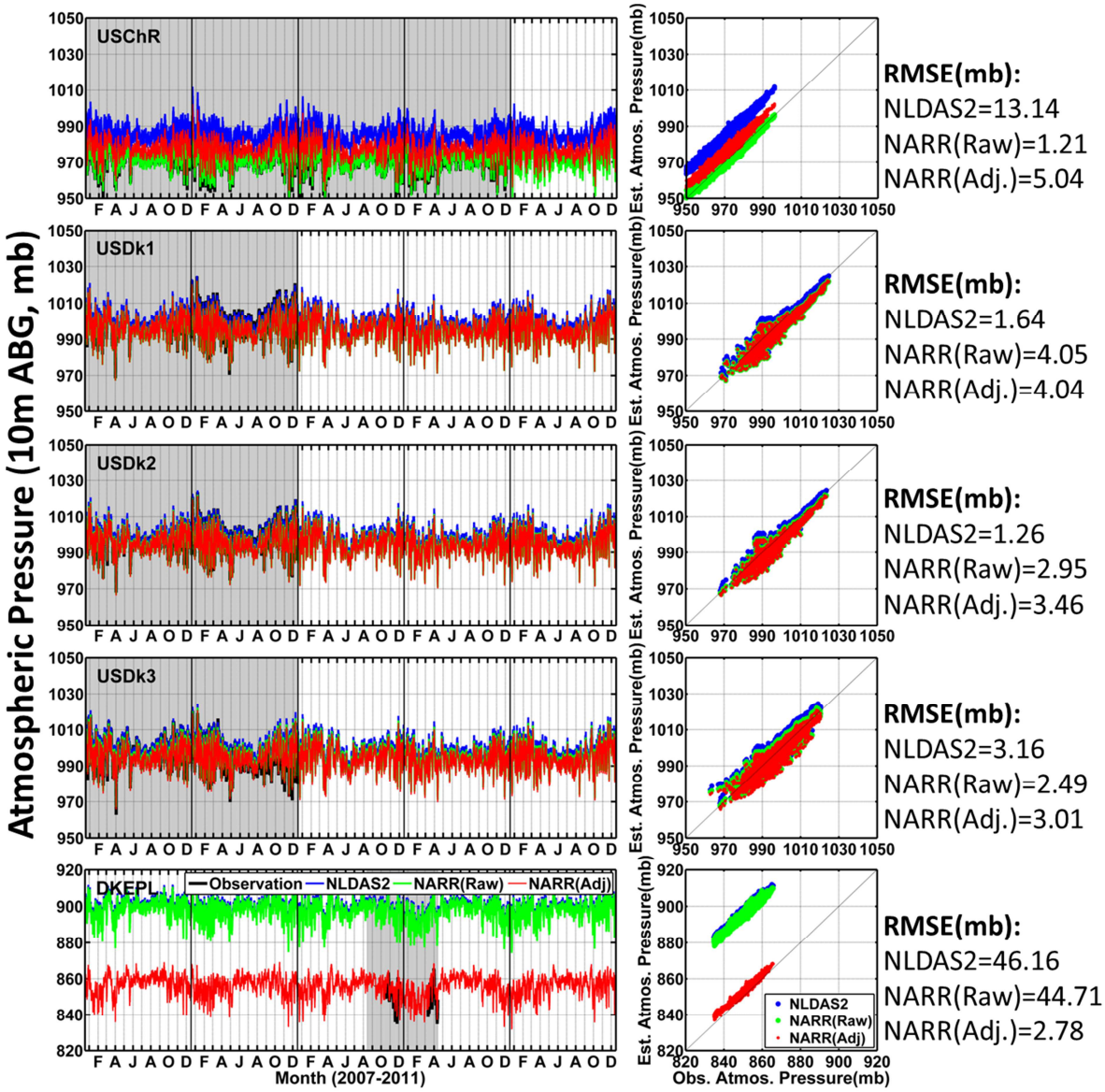

Figure 15 – The comparison between observed and estimated atmospheric pressure from NLDAS2, NARR before (Raw) and after (Adj) elevation correction in the five year period, at four AmeriFlux towers, namely US-ChR, US-Dk1, US-Dk2, US-Dk3, and the DKEPL tower from the top to the bottom, respectively. The shaded windows represent the observation available period.

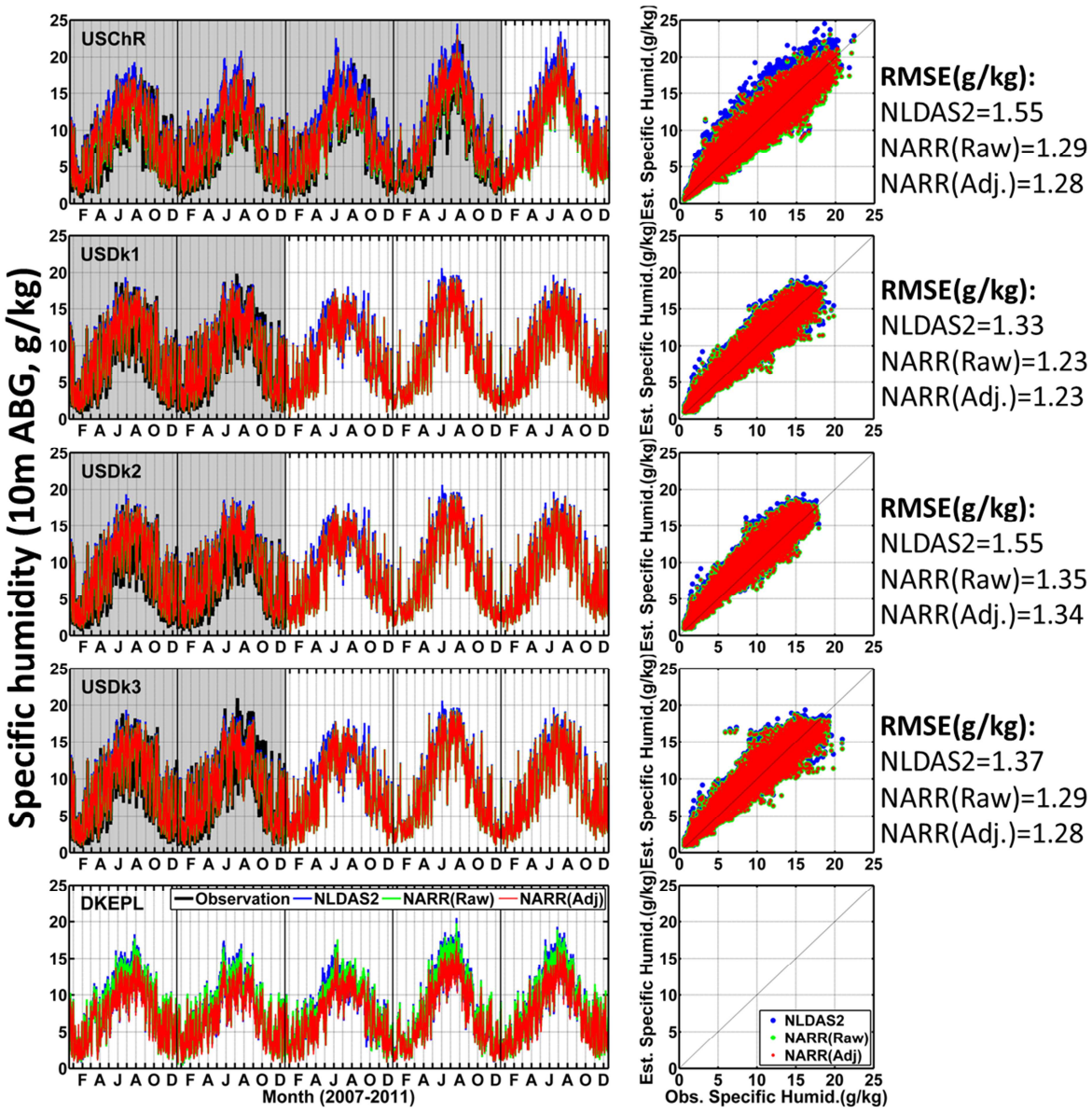

Figure 16 – The comparison between observed and estimated atmospheric specific humidity from NLDAS2, NARR before (Raw) and after (Adj) elevation correction in the five year period, at four AmeriFlux towers, namely US-ChR, US-Dk1, US-Dk2, US-Dk3, and the DKEPL tower from the top to the bottom, respectively. The shaded windows represent the observation available period.

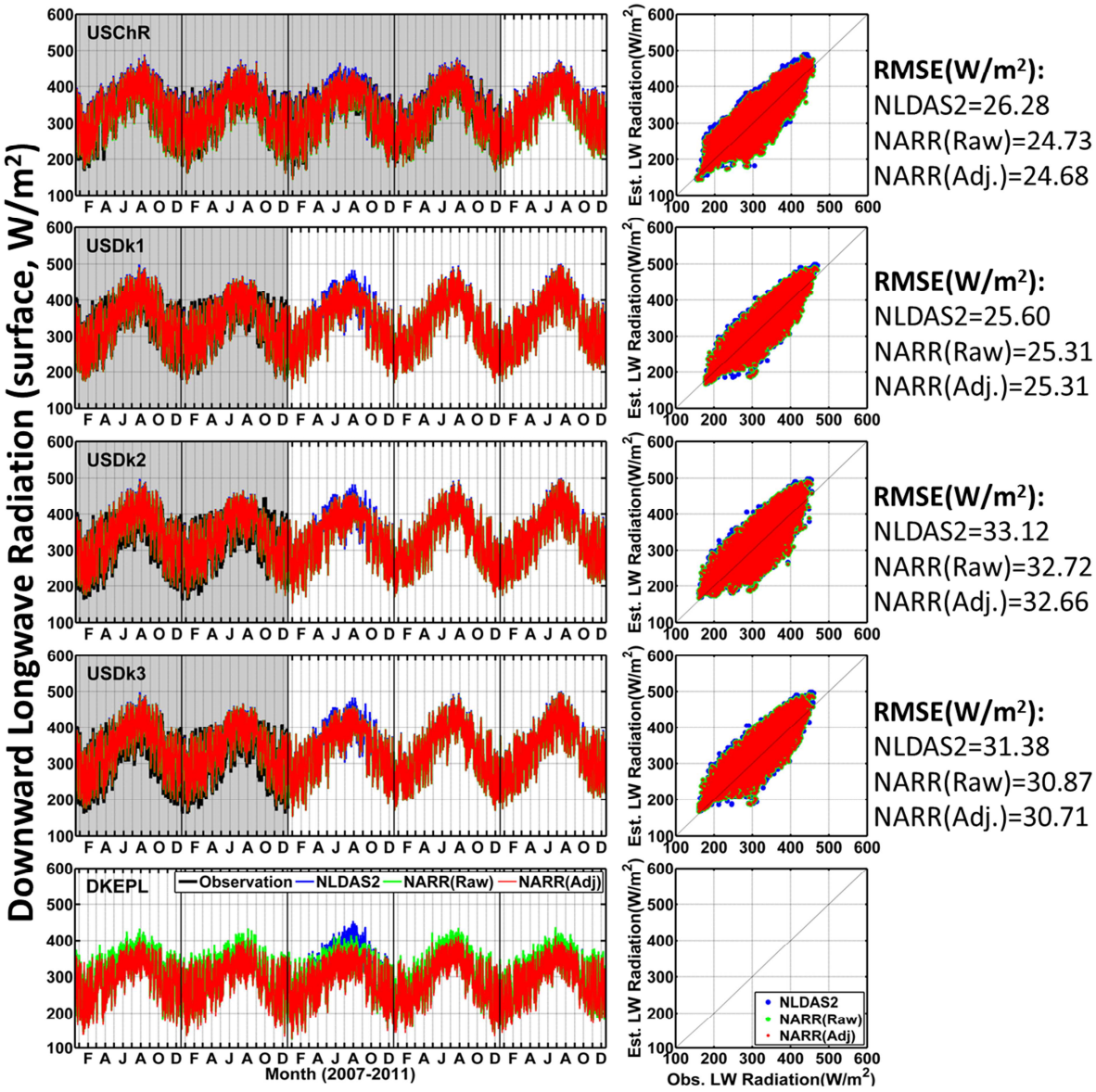

Figure 17 – The comparison between observed and estimated downward longwave radiation at surface from NLDAS2, NARR before (Raw) and after (Adj) elevation correction in the five year period, at four AmeriFlux towers, namely US-ChR, US-Dk1, US-Dk2, US-Dk3, and the DKEPL tower from the top to the bottom, respectively. The shaded windows represent the observation available period.

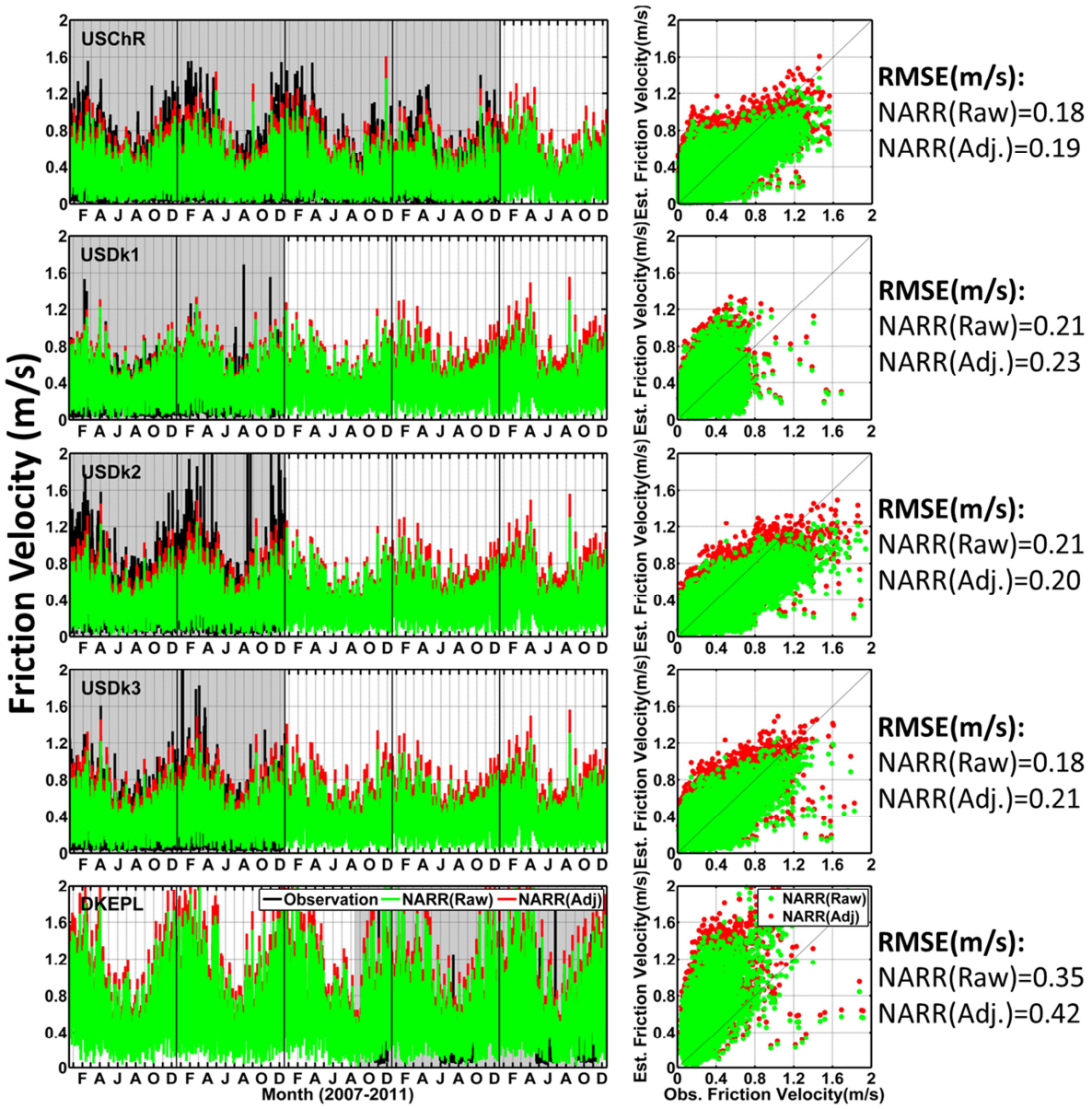

Figure 18 – The comparison between observed and estimated friction velocity near surface from NARR before (Raw) and after (Adj) adjustment in the five year period, at four AmeriFlux towers, namely US-ChR, US-Dk1, US-Dk2, US-Dk3, and the DKEPL tower from the top to the bottom, respectively. The shaded windows represent the observation available period.

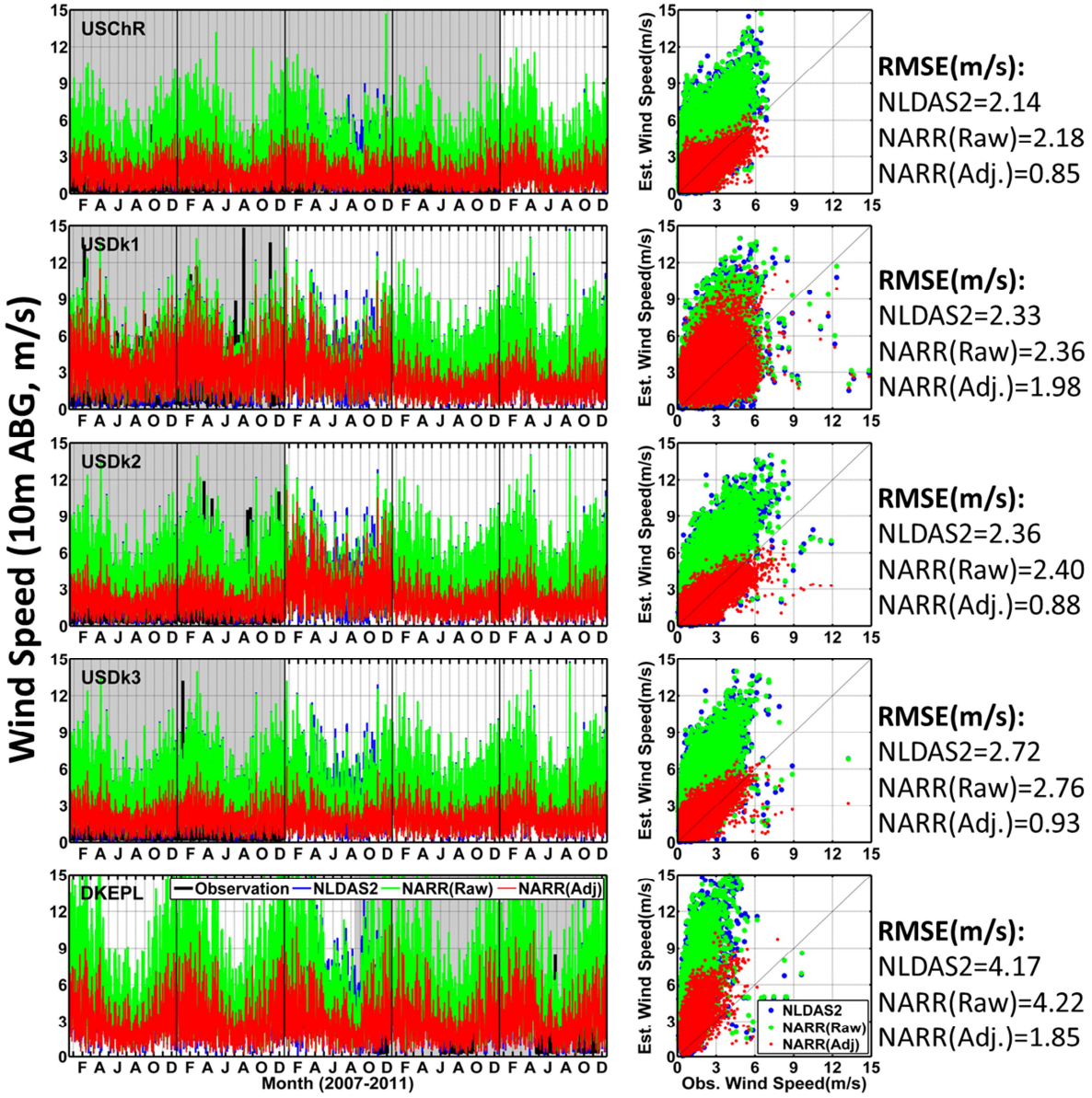

961

962 Figure 19 – The comparison between observed and estimated wind speed at 10m above ground
963 from NLDAS2, NARR before (Raw) and after (Adj) adjustment in the five year period, at four
964 AmeriFlux towers, namely US-ChR, US-Dk1, US-Dk2, US-Dk3, and the DKEPL tower from
965 the top to the bottom, respectively. The shaded windows represent the observation available
966 period.

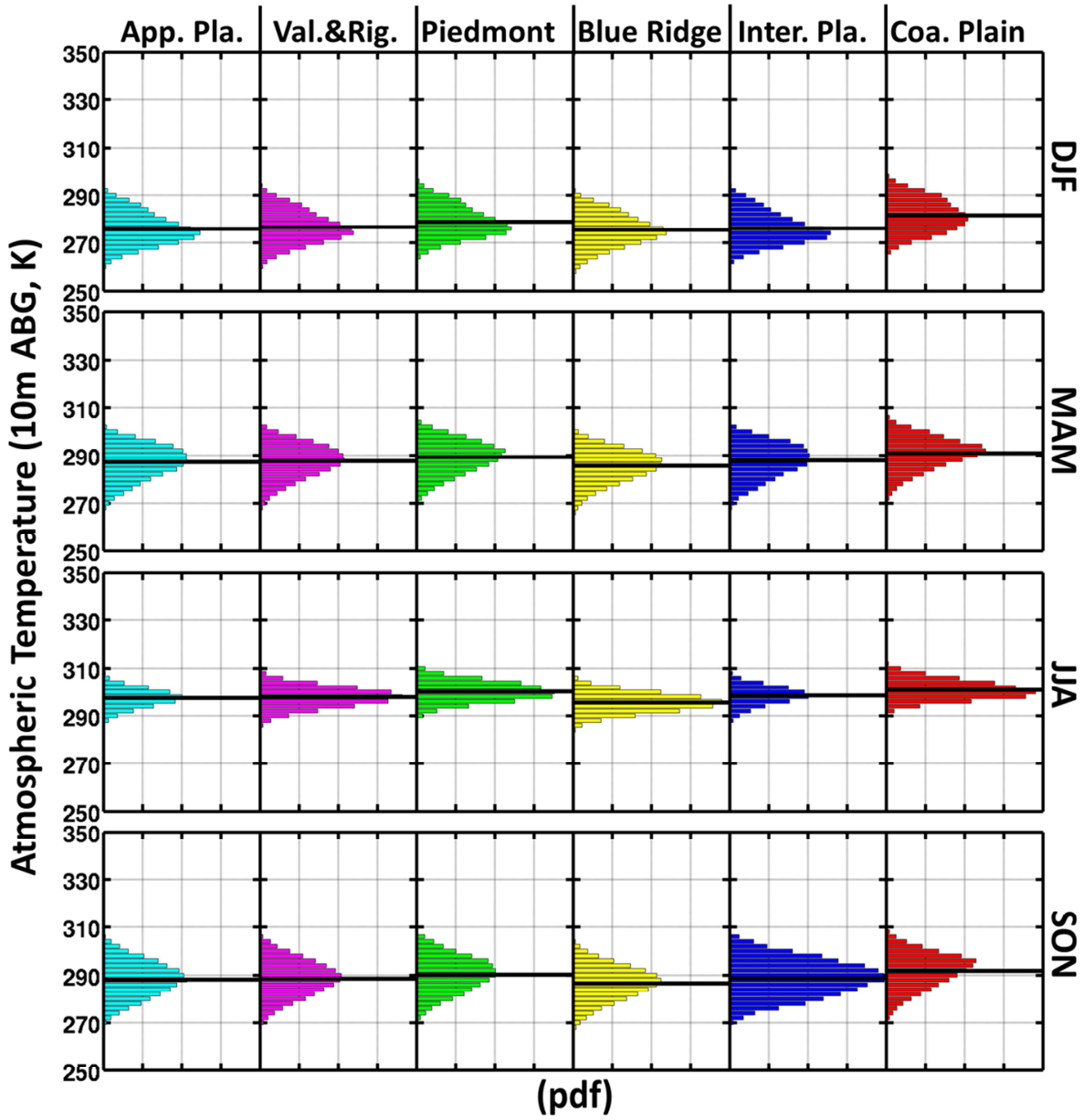

967

968 Figure 20 – PDFs of atmospheric temperature at 10m ABG for each physiographic province,
969 namely Appalachian Plateaus, Valley and Ridge, Piedmont, Blue Ridge, Interior low plateaus
970 and Coastal plain (as shown in Figure 1), and for the four seasons from the top to the bottom,
971 respectively. The horizontal dark bar indicates the mean for each case. All the x-axis is ranging
972 from 0 to1. The maximum pdf used for scaling, as well as the basic statistics is shown in Table 2.

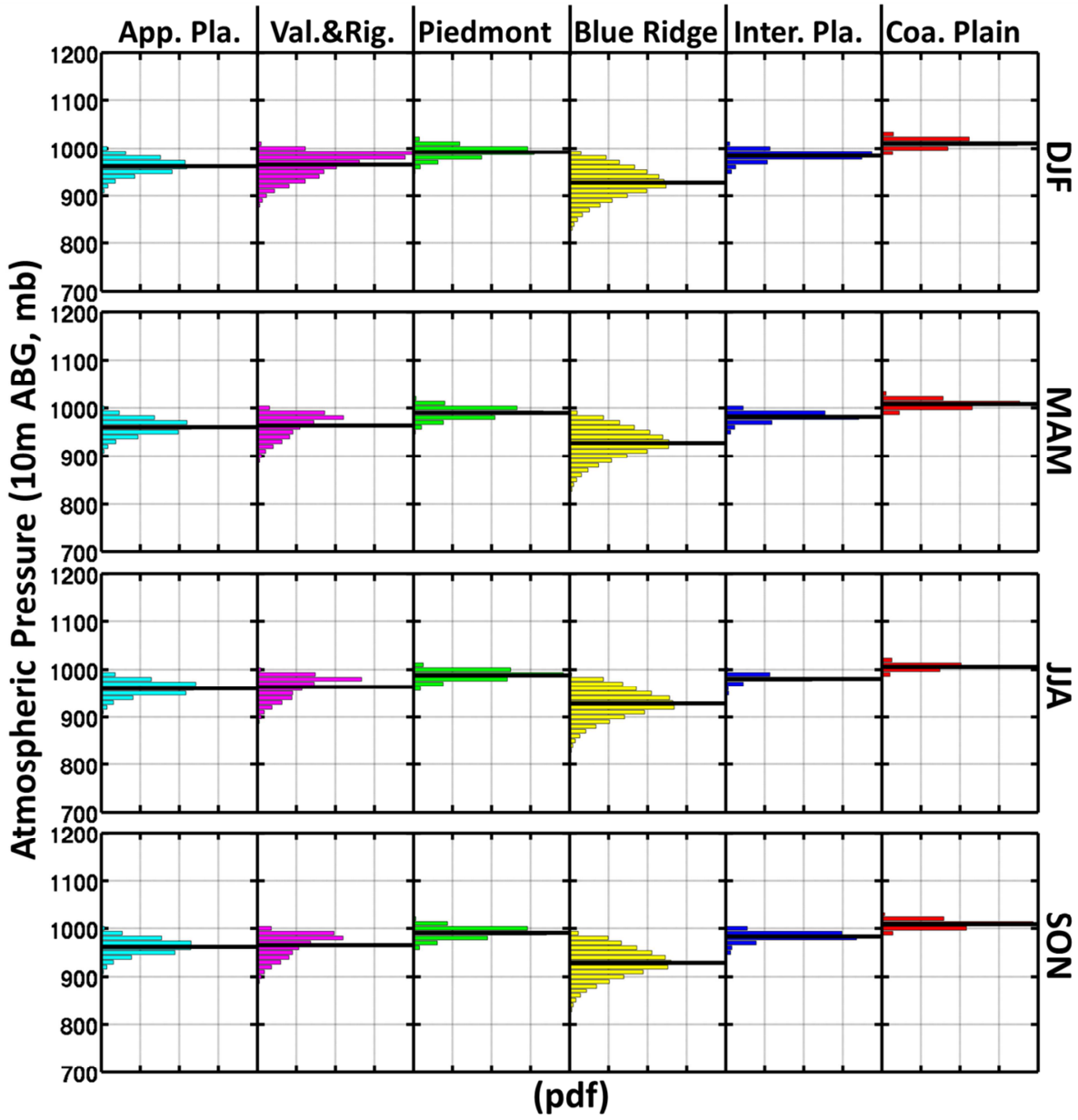

973

974 Figure 21 – PDFs of atmospheric pressure at 10m ABG for each physiographic province, namely
975 Appalachian Plateaus, Valley and Ridge, Piedmont, Blue Ridge, Interior low plateaus and
976 Coastal plain (as shown in Figure 1), and for the four seasons from the top to the bottom,
977 respectively. The horizontal dark bar indicates the mean for each case. All the x-axis is ranging
978 from 0 to1. The maximum pdf used for scaling, as well as the basic statistics is shown in Table 3.

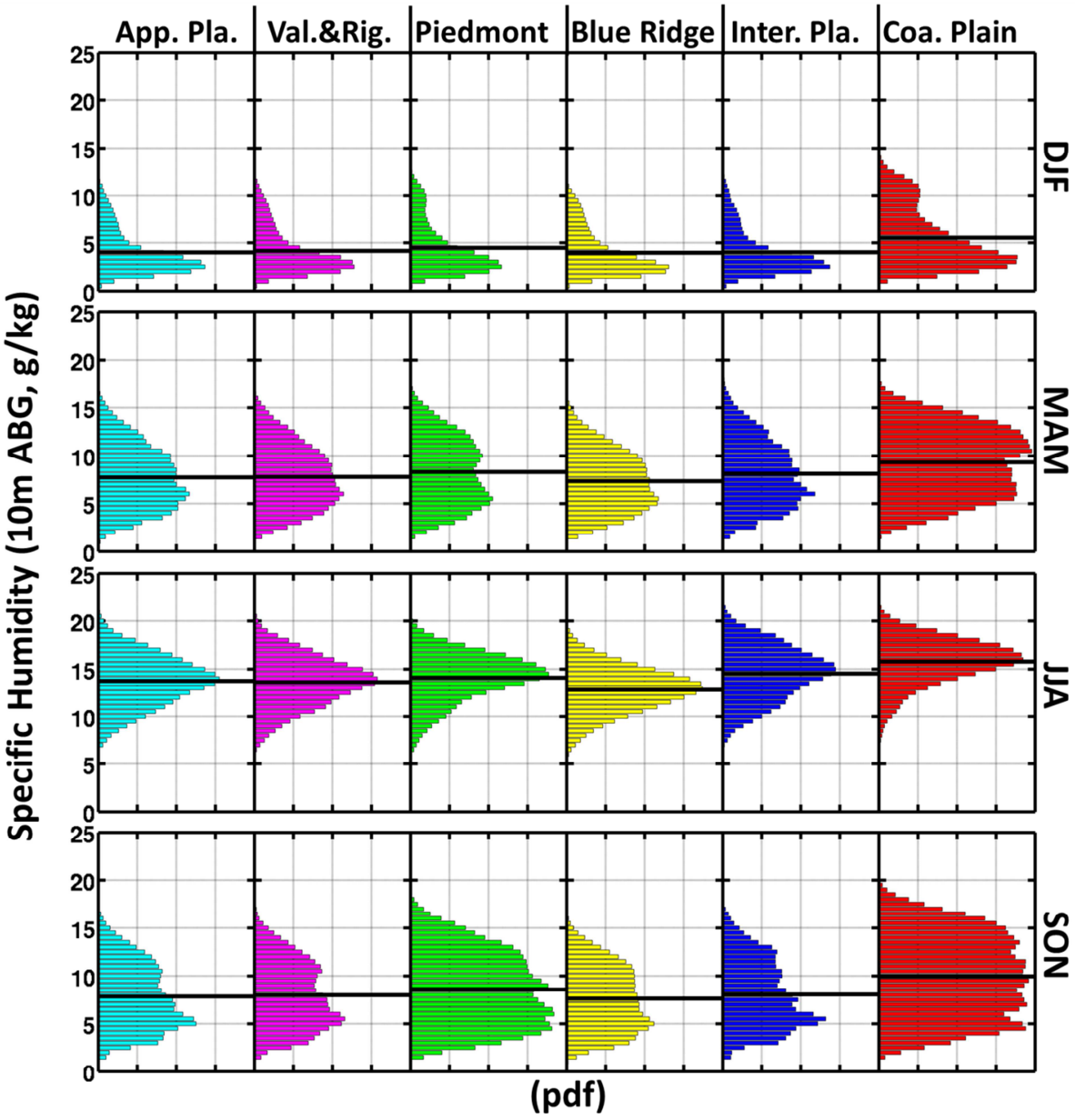

979

980 Figure 22 – PDFs of specific humidity at 10m ABG for each physiographic province, namely
981 Appalachian Plateaus, Valley and Ridge, Piedmont, Blue Ridge, Interior low plateaus and
982 Coastal plain (as shown in Figure 1), and for the four seasons from the top to the bottom,
983 respectively. The horizontal dark bar indicates the mean for each case. All the x-axis is ranging
984 from 0 to1. The maximum pdf used for scaling, as well as the basic statistics is shown in Table 4.

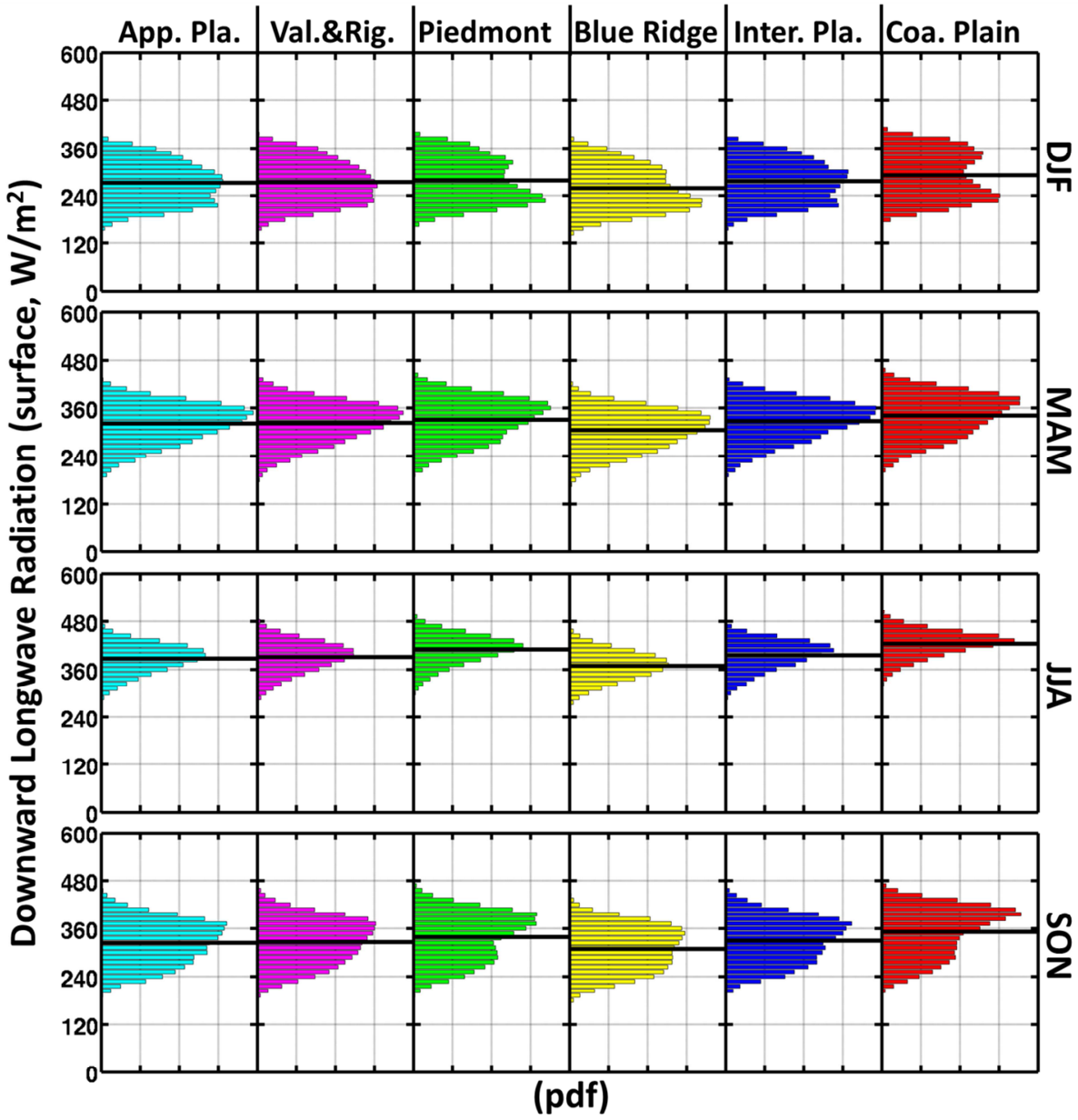

985

986 Figure 23 – PDFs of downward longwave radiation at surface for each physiographic province,
987 namely Appalachian Plateaus, Valley and Ridge, Piedmont, Blue Ridge, Interior low plateaus
988 and Coastal plain (as shown in Figure 1), and for the four seasons from the top to the bottom,
989 respectively. The horizontal dark bar indicates the mean for each case. All the x-axis is ranging
990 from 0 to1. The maximum pdf used for scaling, as well as the basic statistics is shown in Table 5.

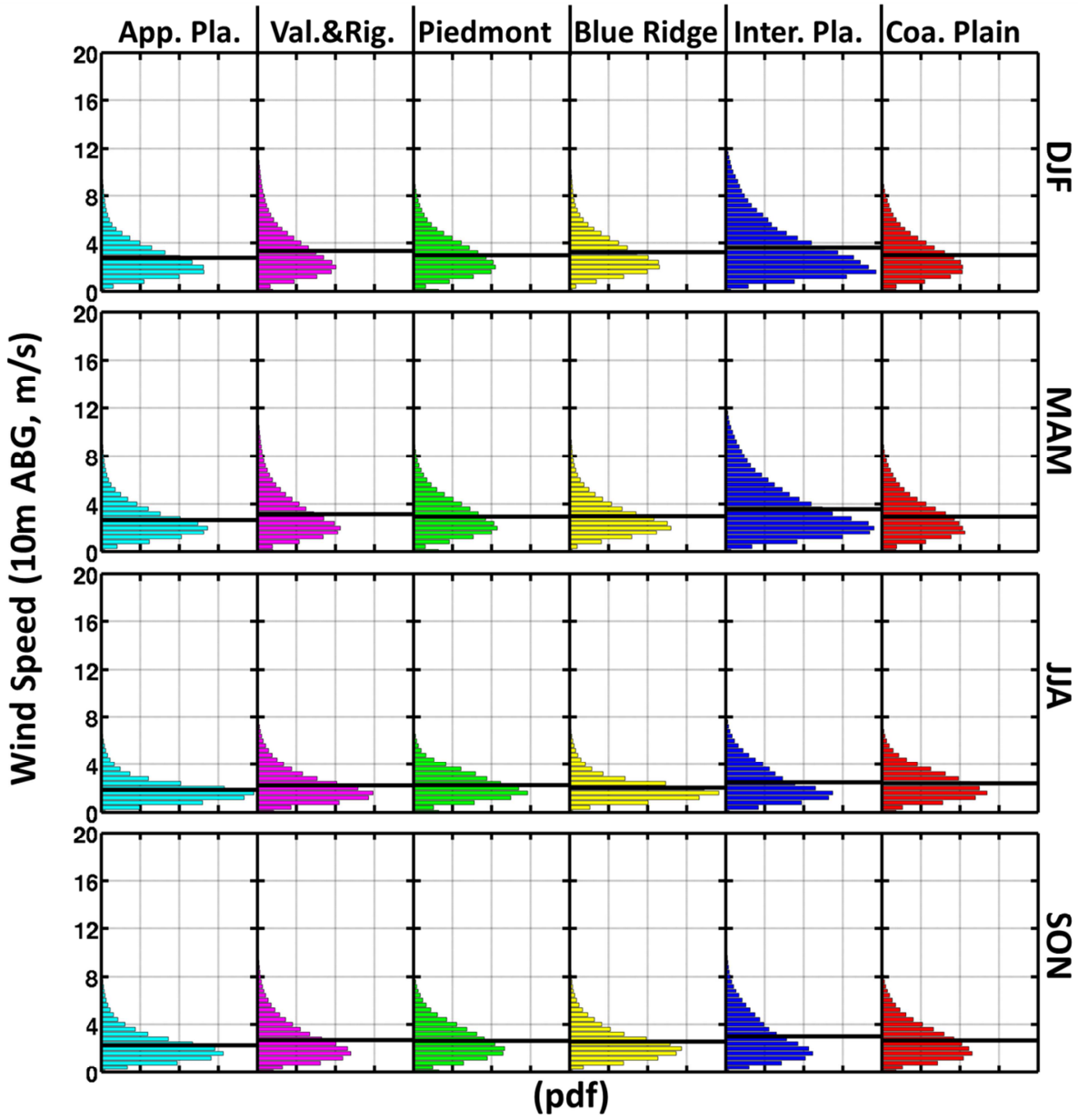

991

992 Figure 24 – PDFs of wind speed at 10m ABG for each physiographic province, namely
993 Appalachian Plateaus, Valley and Ridge, Piedmont, Blue Ridge, Interior low plateaus and
994 Coastal plain (as shown in Figure 1), and for the four seasons from the top to the bottom,
995 respectively. The horizontal dark bar indicates the mean for each case. All the x-axis is ranging
996 from 0 to1. The maximum pdf used for scaling, as well as the basic statistics is shown in Table 6.

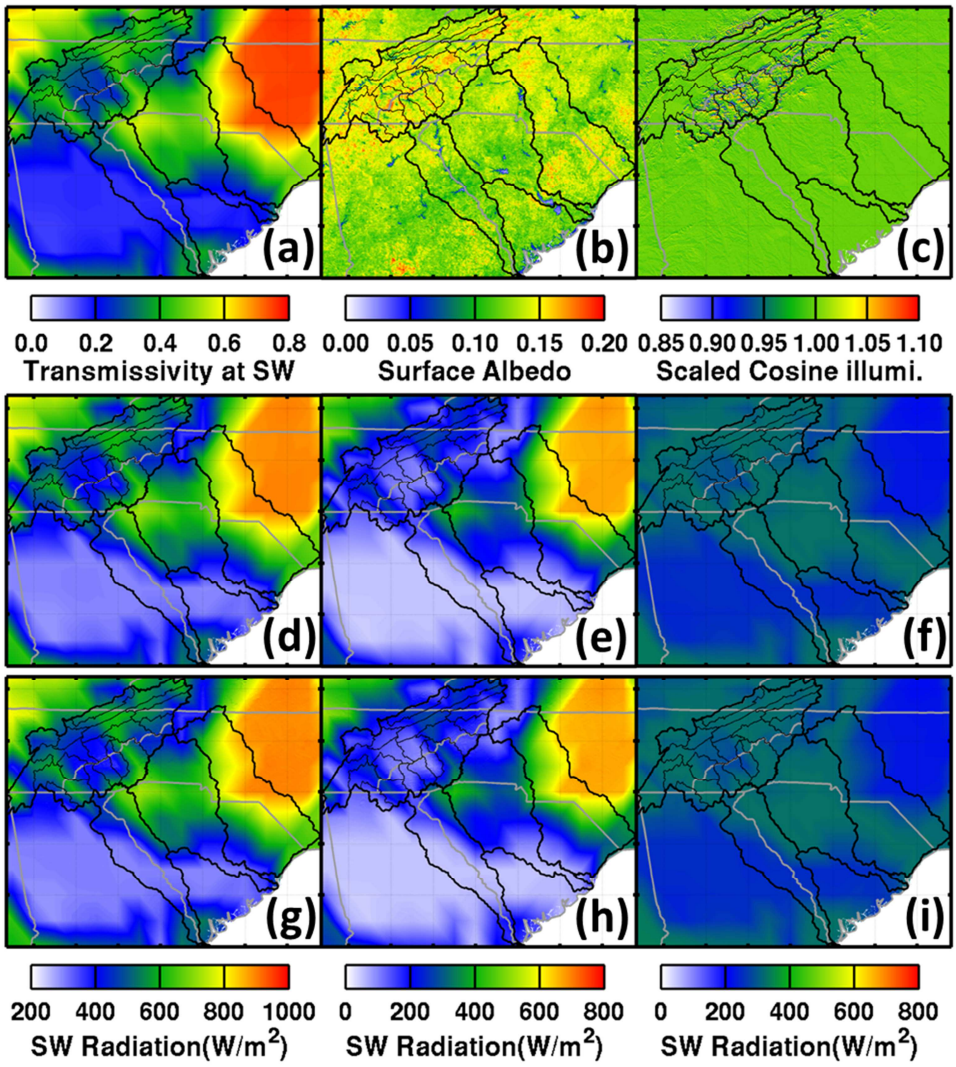

997

998 Figure 25 – The time-variant auxiliary input parameters, including the derived transmittance at
999 shortwave (a), surface albedo (b) and the scaled cosine of local illumination angle (c) over the
1000 SE US at 1pm on Sep. 1, 2009 from left to right. The figures in the middle raw show the NARR
1001 total incoming SW radiation after cloudiness correction (d), and the direct (e) and diffuse (f)
1002 components partitioned from the cloudiness corrected total SW radiation using the transmittance
1003 (a). The figure at the bottom row show the cloudiness and topographically corrected total SW
1004 radiation (g), the sum of direct and reflected components (h), and the diffuse component (i) of
1005 the final corrected radiation (g).

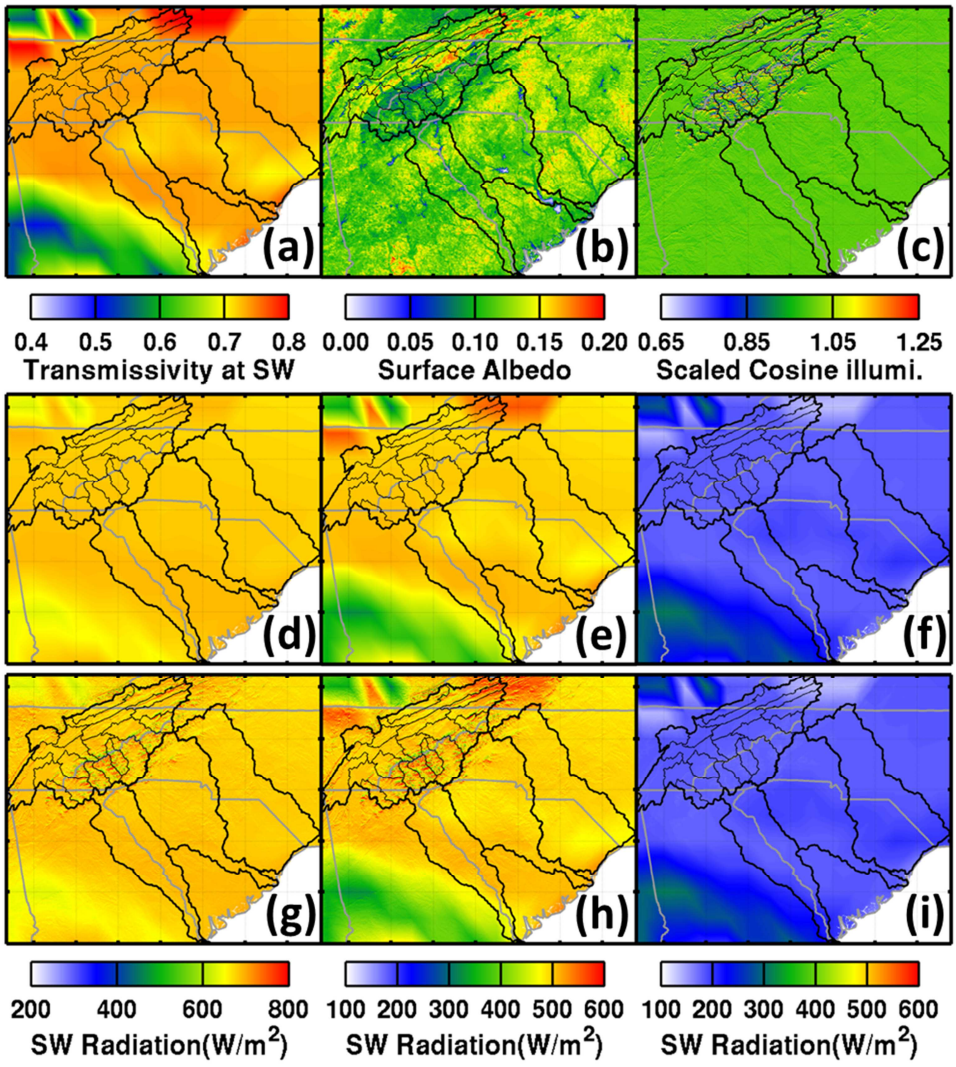

1006

1007 Figure 26 – The time-variant auxiliary input parameters, including the derived transmittance at
1008 shortwave (a), surface albedo (b) and the scaled cosine of local illumination angle (c) over the
1009 SE US at 1pm on Feb. 1, 2009 from left to right. The figures in the middle raw show the NARR
1010 total incoming SW radiation after cloudiness correction (d), and the direct (e) and diffuse (f)
1011 components partitioned from the cloudiness corrected total SW radiation using the transmittance
1012 (a). The figure at the bottom row show the cloudiness and topographically corrected total SW
1013 radiation (g), the sum of direct and reflected components (h), and the diffuse component (i) of
1014 the final corrected radiation (g).

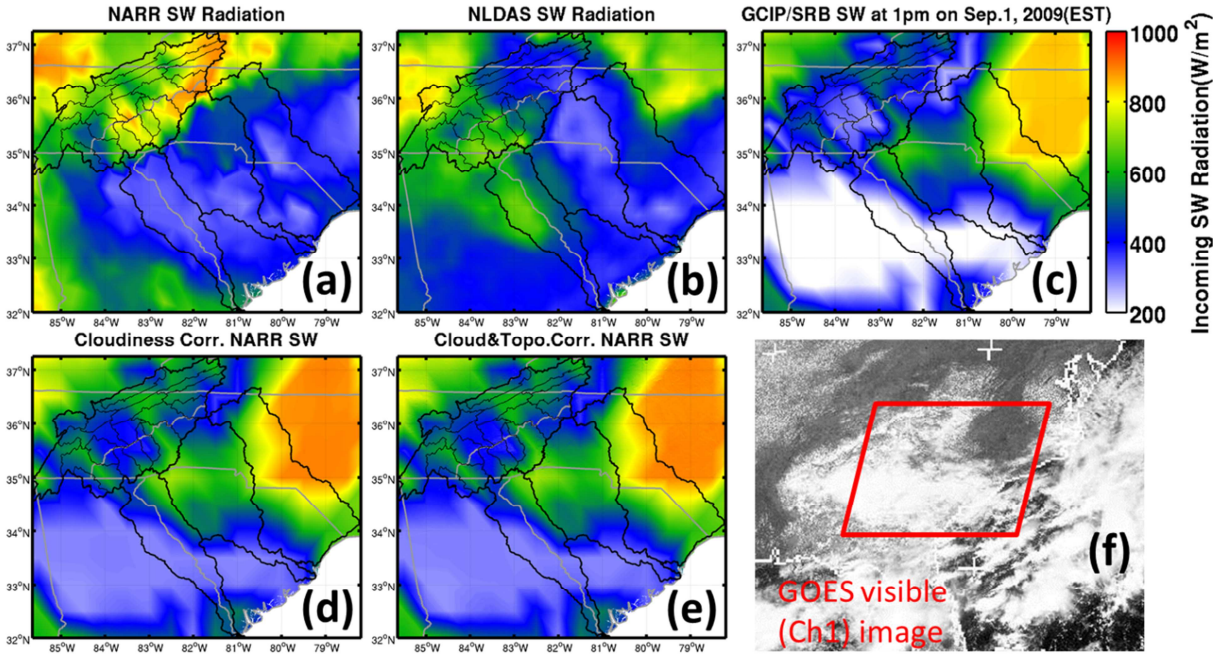

Figure 27 – Comparison of the downward shortwave radiation between the NARR total incoming SW radiation before any correction (a), the NLDAS2 field (b), the SRB-GCIP solar radiation (c), the NARR SW radiation after cloudiness correction (d) and after both cloudiness and topographic correction (e) for a **cloudy** situation at 1pm on Sep. 1, 2009; (f) is the GOES visible (Channel 1) image, demonstrating the cloudiness pattern.

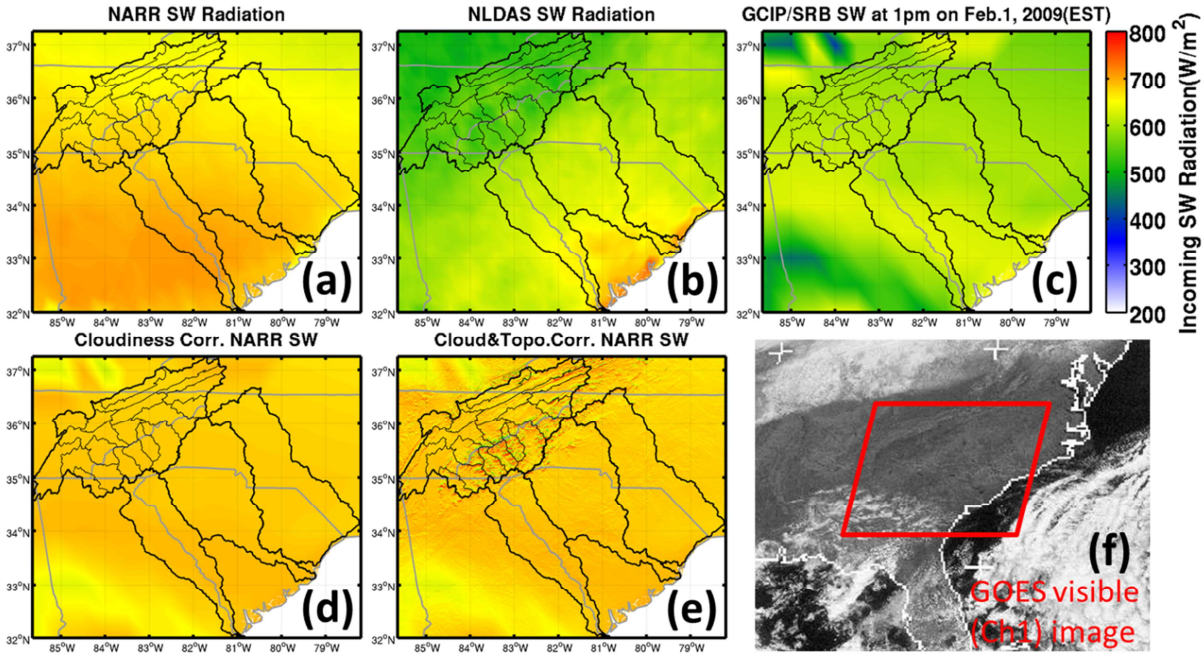

1022

1023 Figure 28 – Comparison of the downward shortwave radiation between the NARR total
1024 incoming SW radiation before any correction (a), the NLDAS2 field (b), the SRB-GCIP solar
1025 radiation (c), the NARR SW radiation after cloudiness correction (d) and after both cloudiness
1026 and topographic correction (e) for a **clear** situation at 1pm on Feb. 1, 2009; (f) is the GOES
1027 visible (Channel 1) image, demonstrating the sky is almost clear except for the southwest corner.

1028

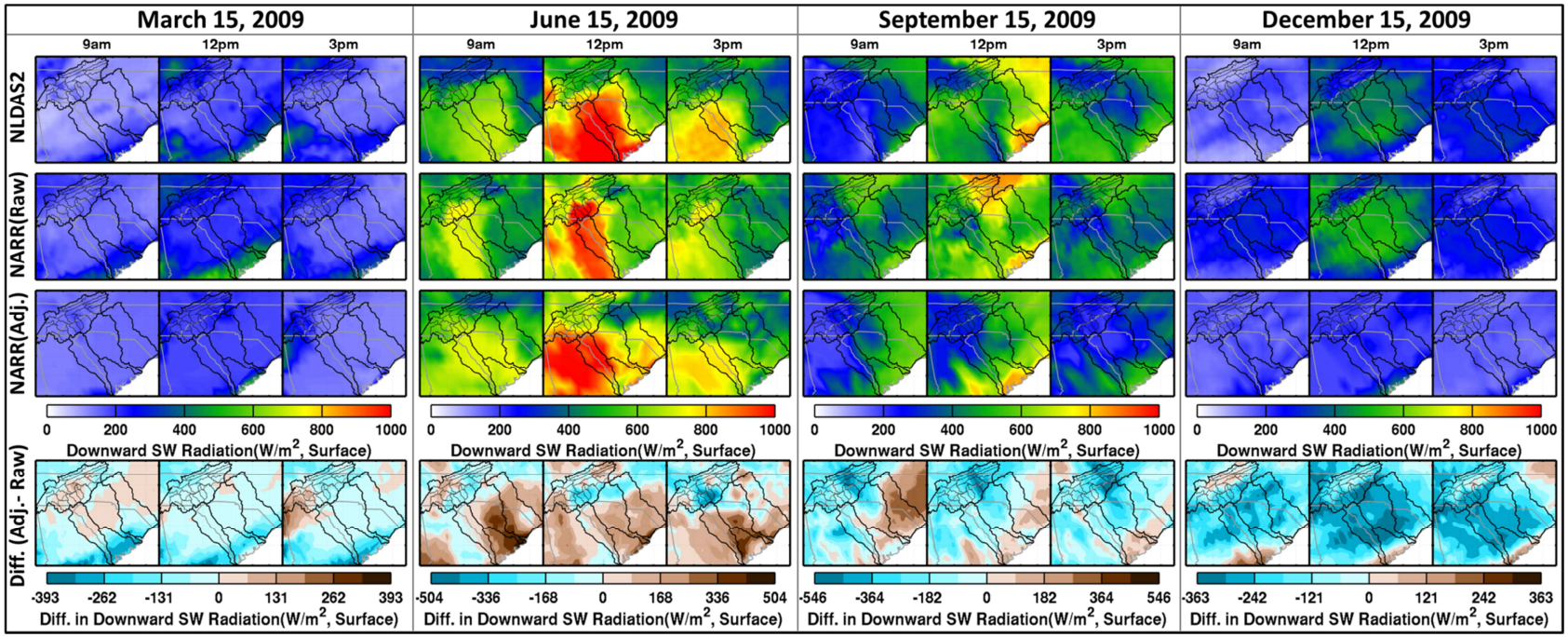

Figure 29 – The downward shortwave radiation at surface over the SE US from NLDAS2, NARR before (Raw) and after (Adj) cloudiness and topographic correction at 9am, noon and 3pm (EST) on Mar. 15, Jun. 15, Sep. 15, and Dec. 15 in 2009 from the left to the right, respectively. The bottom figures show the difference between the NARR downward shortwave radiation after and before corrections, using a symmetrical blue-brown color scale such that the brown color represents positive values and the blue color represent negative values.

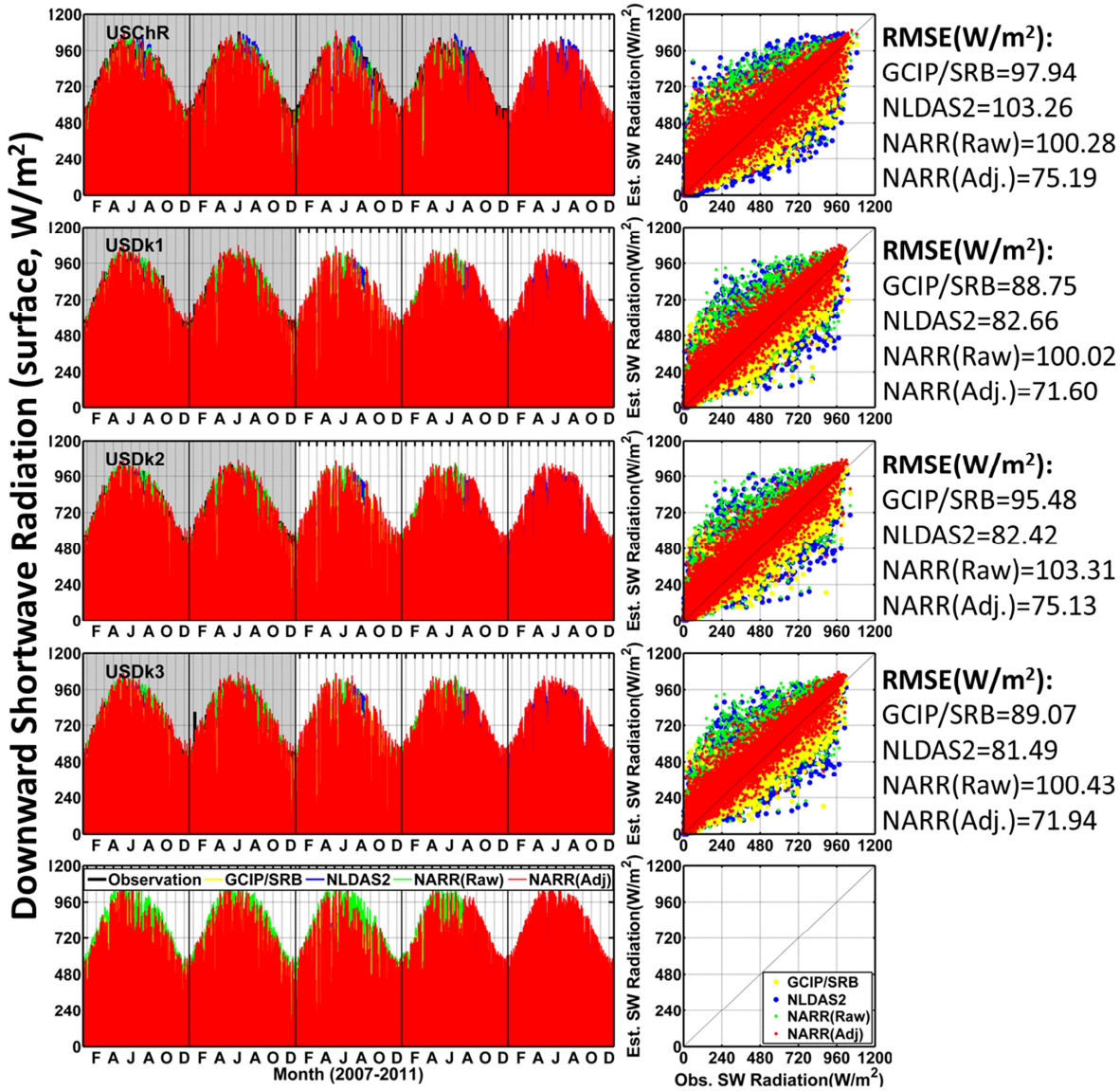

Figure 30 – The comparison between observed and estimated hourly downward shortwave radiation at surface from GCIP/SRB, NLDAS2, the hourly SW radiation temporally interpolated from 3-hour NARR SW radiation based on the solar zenith angle (Raw), and the hourly NARR SW radiation after cloudiness and topographic correction (Adj) in the five year period, at four AmeriFlux towers including US-ChR, US-Dk1, US-Dk2, US-Dk3, and the DKEPL tower from the top to the bottom, respectively. The shaded windows represent the observation available period.

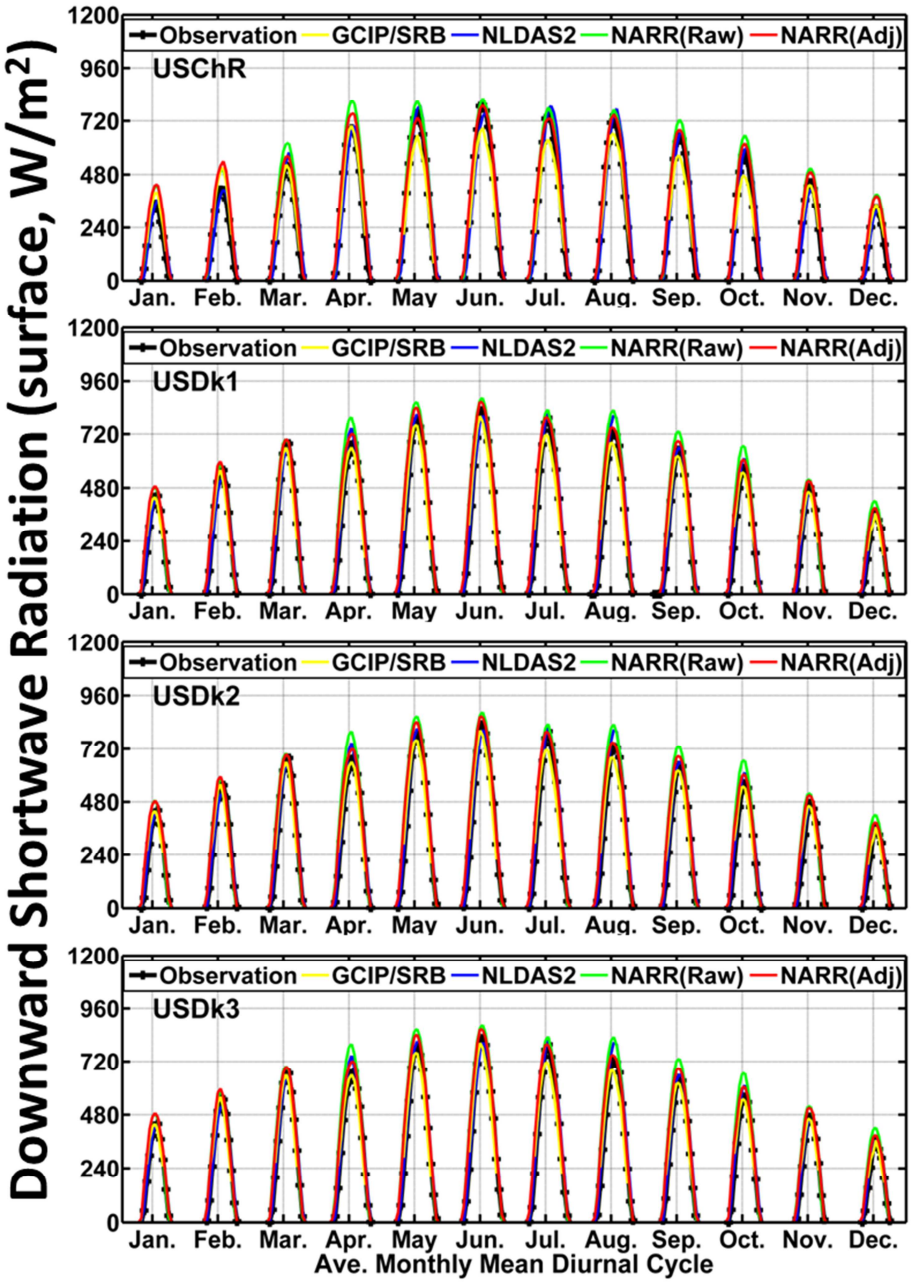

1043

1044 Figure 31 – Comparison of the monthly mean diurnal cycle of incoming solar radiation
1045 calculated using hourly SW radiation temporally interpolated from 3-hour NARR SW radiation
1046 based on the solar zenith angle (Raw), and the hourly NARR SW radiation after cloudiness and
1047 topographic correction (Adj), as well as the hourly SW radiation from NLDAS2 and SRB-GCIP,
1048 at AmeriFlux towers including USChR, USDk1, USDk2 and USDk3.